PHYSICAL REVIEW B **107**, 045143 (2023)

Instanton gas approach to the Hubbard model

Maksim Ulybyshev,[1,*] Christopher Winterowd,[2,†] Fakher Assaad,[1,3,‡] and Savvas Zafeiropoulos[4,§]
[1]*Institute for Theoretical Physics, Julius-Maximilians-Universität Würzburg, 97074 Würzburg, Germany*
[2]*Johann Wolfgang Goethe-Universität Frankfurt am Main, Frankfurt am Main, Germany*
[3]*Würzburg-Dresden Cluster of Excellence ct.qmat, Julius-Maximilians-Universität Würzburg, 97074 Würzburg, Germany*
[4]*Aix Marseille Univ, Université de Toulon, CNRS, CPT, Marseille, France*

(Received 9 August 2022; revised 22 December 2022; accepted 23 December 2022; published 30 January 2023)

In this paper, we consider a path integral formulation of the Hubbard model based on a Hubbard-Stratonovich transformation that couples the auxiliary field to the local electronic density. This decoupling is known to have a saddle-point structure that shows a remarkable regularity: The field configuration at each saddle point can be understood in terms of a set of elementary field configurations localized in space and imaginary time which we coin instantons. The interaction between instantons is short ranged. Here, we formulate a classical partition function for the instanton gas that has predictive power. For a given set of physical parameters, we can predict the distribution of instantons and show that the instanton number is sharply defined in the thermodynamic limit, thereby defining a unique dominant saddle point. Decoupling in the charge channel conserves SU(2) spin symmetry for each field configurations. Hence, the instanton approach provides an SU(2) spin-symmetric approximation to the Hubbard model. It fails, however, to capture the magnetic transition inherent to the Hubbard model on the honeycomb lattice despite being able to describe local moment formation. In fact, the instanton itself corresponds to local moment formation and concomitant short-ranged antiferromagnetic correlations. This aspect is also seen in the single particle spectral function that shows clear signs of the upper and lower Hubbard *bands*. Our instanton approach bears remarkable similarities to local dynamical approaches, such as dynamical mean-field theory, in the sense that it has the unique property of allowing for local moment formation without breaking the SU(2) spin symmetry. In contrast to local approaches, it captures short-ranged magnetic fluctuations. Furthermore, it also offers possibilities for systematic improvements by taking into account fluctuations around the dominant saddle point. Finally, we show that the saddle point structure depends upon the choice of lattice geometry. For the square lattice at half filling, the saddle-point structure reflects the itinerant to localized nature of the magnetism as a function of the coupling strength. The implications of our results for Lefschetz thimble approaches to alleviate the sign problem are also discussed.

DOI: 10.1103/PhysRevB.107.045143

I. INTRODUCTION

A strong local Coulomb repulsion between electrons leads to the localization of charge degrees of freedom and to the formation of local magnetic moments. As shown in Anderson's seminal paper [1], local moment formation in metals can be captured at the mean-field level by breaking the spin-rotational symmetry. Generically, however, local moment formation is a dynamical effect in which the net moment averages to zero over time, thus restoring the spin-rotational symmetry. The success of the so-called dynamical mean-field theory (DMFT) [2,3] is that it captures this phenomena. Local moment formation and the associated short-range magnetic fluctuations in metals present a key challenge in the understanding of strongly correlated electron systems and has important implications for the understanding of transition metal oxides such as high-temperature superconductors [4] or rare-earth heavy fermion materials [5,6].

The aim of this paper is to provide a framework that captures local moment formation in metallic environments. In contrast to DMFT, both temporal and spatial fluctuations will be taken into account. We will concentrate on the Hubbard model on square and honeycomb lattices, working within a path-integral formulationto derive our approximation from the saddle-point structure. Clearly, the path-integral formulation of the Hubbard model on a given lattice is not unique and the saddle-point structure will depend on the specific treatment of the interaction term. For instance, one can use a decoupling where the real scalar field couples to the local magnetization. As a consequence, the saddle-point structure will correspond to states where the spin symmetry is broken. However, if the integration over the scalar field is carried out exactly, the final result will be spin-rotational symmetric and independent of the decoupling channel.

As we want to describe local moment formation without explicitly breaking the spin symmetry, we will adopt a path-integral formulation where a real space- and time-dependent scalar field couples to the local charge degree of freedom. For this choice of Hubbard-Stratonovich (HS) transformation,

---

[*] Maksim.Ulybyshev@physik.uni-wuerzburg.de
[†] winterowd@itp.uni-frankfurt.de
[‡] Fakher.Assaad@physik.uni-wuerzburg.de
[§] Savvas.Zafeiropoulos@cpt.univ-mrs.fr

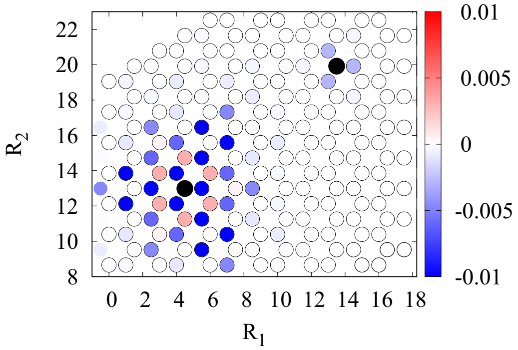

FIG. 1. Spin-spin correlations, $\frac{1}{3}\langle \hat{\boldsymbol{S}}_{\boldsymbol{x}_0}(T)\cdot \hat{\boldsymbol{S}}_{\boldsymbol{x}_0+\boldsymbol{x}}(T)\rangle$, for a field configuration with one instanton at space time (X, T). We consider two values of $\boldsymbol{x}_0$. The left black circle corresponds to $\boldsymbol{x}_0 = X$. The other value of $\boldsymbol{x}_0$ (right black circle) is far from the instanton. R_1 and R_2 are two Cartesian coordinates of the lattice sites, displayed in the units of the distance between nearest neighbors. These calculations were performed on a 12×12 lattice at interaction strength $U = 2.0\kappa$ (see Secs. II A and II B for the notation).

SU(2) spin symmetry is present for all field configurations. Solving the saddle-point equations under the assumption of fields which are constant in space and time reduces to the paramagnetic mean-field approximation to the Hubbard model [7] in which the field vanishes.

We would like to go beyond this trivial solution and, in particular, provide a map of all saddle points without the restriction to fields which are constant in space and time. We note that since the action is not necessarily real, one generically has to continue the real scalar field to the complex plane to achieve this goal. The motivation to do so is at least twofold. On one hand, the saddle point structure is necessary to formulate the so-called Lefschetz thimble decomposition [8,9] that has the potential of alleviating the severity of the negative sign problem [10,11]. In particular, each thimble is attached to a saddle point, and the imaginary part of the action is constant within the thimble. On the other hand, the very structure of the (complex) saddle points can yield valuable approximation schemes that can be improved at will. Here we will consider the latter but concentrate on cases where the action is real, as realized at the particle-hole symmetric point. In this case, the complexification of the field is not required.

Finding saddle points is a daunting task. Here we use auxiliary field quantum Monte Carlo simulations to sample the fields, and for each independent configuration, stop the Monte Carlo sampling and integrate the steepest descent differential equation so as to flow to the saddle point. This provides a complete map. Remarkably, as was shown in Ref. [12], for the honeycomb lattice at any coupling and for the square lattice at strong coupling, the saddle-point structure is quite regular. All saddles can be understood in terms of an elementary configuration, an instanton, in which the fields differs from zero only in a small space-time region. Physically, it corresponds to the formation of a local moment at a given space-time point and concomitant short-ranged antiferromagnetic (AFM) fluctuations around this point (see Fig. 1). Under the assumption of spatial locality, and as shown in Appendix B, the instanton is characterized by a topological winding number

This instanton approach provides an interesting link between the structure of the path integral for the Hubbard model and long-established methods in quantum chromodynamics (QCD). Instantons were introduced almost 50 years ago in the context of Yang-Mills theory [13] and are defined as topologically nontrivial solutions of the classical field equations in Euclidean space with finite action. They very quickly found many applications even in quantum mechanics, where they describe the tunneling processes from one vacuum to another. This is also the case in Yang-Mills theories where they describe tunneling processes between different degenerate vacua which are labeled by different values of the winding number, a topological index. In the context of QCD, they play an important role in the explanation of the mechanism of spontaneous breaking of chiral symmetry and applications of instantons can be found in the solution of the U(1) problem and the strong CP problem. Beyond the context of strong interactions, instantons have related counterparts in the electroweak sector, where the so-called sphalerons can lead to processes that violate the baryon and lepton number conservation and could potentially describe rare processes of baryon decay. The instanton calculus has proven to be extremely powerful in supersymmetric gauge theories where it allowed for example the calculation of the exact β function. For more details on field theoretical applications, we refer the interested reader to Refs. [14,15]. Beyond physics, instantons also have fascinating applications in mathematics where, for example, they can be used for the classification of four-manifolds [16].

Returning to QCD, the introduction of the concept of an instanton led to the modeling of the QCD partition function as a gas of instantons [17] that could allow for analytical treatment. Later, however, it was understood that correlations between instantons are extremely important for numerous phenomena in QCD and one is forced to go beyond the mean-field approximation and study numerically a liquid of instantons where the ’t Hooft interaction is included to all orders [18]. Guided by these ideas, we will try to adapt this approach in the framework of the Hubbard model to demonstrate that this kind of approximations can lead to interesting and highly nontrivial results in strongly correlated electron systems.

The key result of the paper is that we can define a classical model of the instanton gas that reproduces the saddle-point structure of the path integral for the Hubbard model for a HS field coupling to the charge density. The only inputs needed to completely define this classical model are the characteristics of a single instanton and the two-body interaction between these semiclassical objects. This description of the physics of instantons through a pairwise short-ranged interaction appears naturally through an analysis of the one- and two-instanton configurations. With *simple* classical simulations, we can then generate saddle-point field configurations, which can then determine physical properties of the Hubbard model.

Before plunging into the technical details of the approach we summarize our key results. Figure 1 shows the connection between the instanton and enhanced short-ranged AFM correlations. Here we consider a configuration with a single instanton saddle point, with the instanton located at the space-time point (X, T). We then plot the spin-spin correlations $\frac{1}{3}\langle \hat{\boldsymbol{S}}_{\boldsymbol{x}_0}(T)\cdot \hat{\boldsymbol{S}}_{\boldsymbol{x}_0+\boldsymbol{x}}(T)\rangle$, where $\hat{\boldsymbol{S}}_{\boldsymbol{x}}$ is the spin operator. One will see that for $\boldsymbol{x}_0 = X$ (lower left black circle), substantial

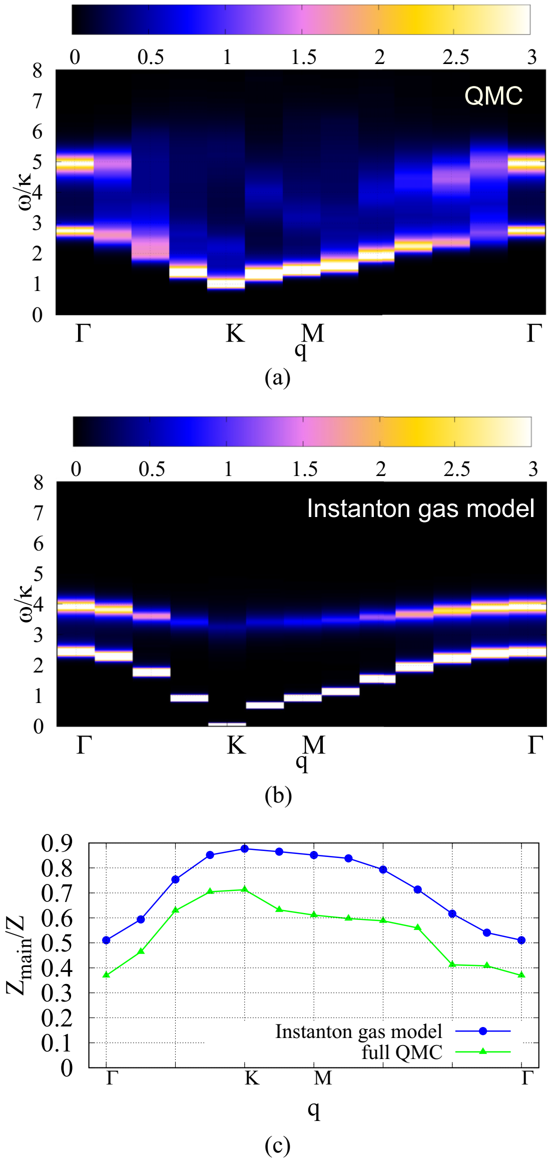

(a)

(b)

(c)

FIG. 2. (a) Spectral functions in momentum space using the ALF [19] implementation of the auxiliary field QMC. (b) The same spectral functions obtained with instanton gas model. (c) The share of the lower peak in the overall spectral weight along the same profile in momentum space. Calculations were done for 12×12 lattice with $N_\tau = 256$ and $\beta\kappa = 20$ (see Secs. II A and II B for the notation). The interaction strength is equal to $U = 6.0\kappa$, which is equal to the bandwidth.

short-ranged correlations are present. On the other hand, *far* from the instanton, where $\boldsymbol{x}_0$ corresponds to the upper right black circle, no AFM order is observed beyond one lattice site.

We expect local moment formation to show up as upper Hubbard *bands* in the single-particle spectral function. Figure 2 shows a comparison of results for this quantity between the instanton gas approach and a full auxiliary field QMC simulation [20,21] for the Hubbard model on the honeycomb lattice in the magnetically ordered phase at $U/U_c = 1.6$, where U_c denotes the critical value of the interaction where antiferromagnetism sets it and a mass gap is generated [22,23]. Our instanton approach does not capture the SU(2) symmetry breaking and hence no mass gap is generated at the Dirac point $\boldsymbol{k} = K$. However, local moment formation and concomitant short-ranged AFM correlations capture the high-energy properties, encoded in the so-called upper Hubbard band.

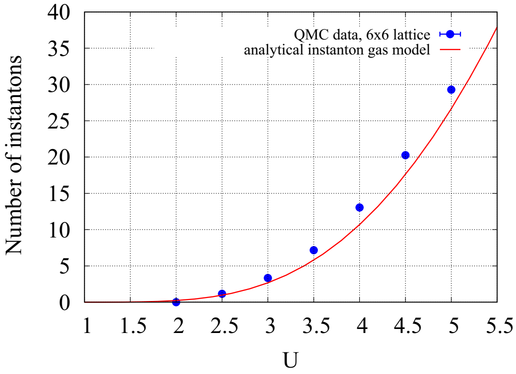

FIG. 3. A comparison of the average number of instantons obtained from real QMC data with the analytical instanton gas model. The QMC data corresponds to a 6×6 spatial size, with $N_\tau = 512$ and $\beta\kappa = 20$.

Finally, Fig. 3 shows that the instanton number obtained in the QMC simulation and in the analytical instanton gas model show very good agreement. Thus, the instanton gas model can be used to predict the dominant saddle point without performing costly QMC simulations.

The paper is organized as follows: in Sec. II, we give a brief description of the specific path integral formulation for the Hubbard model employed in this paper. We also give a short introduction to the Lefschetz thimble formalism. Section III is devoted to the description of the structure of the saddle points for the Hubbard model on the hexagonal lattice. This includes a detailed account of the one-instanton as well as many-instanton solutions. Section IV covers the construction of a semianalytical instanton gas model. In Sec. V, we describe the physics following from the instanton gas model. The last section (Sec. VI) presents preliminary results for the saddle-point approximation to the Hubbard model on the square lattice which is relevant for high-T_c superconductivity. We have included Appendices that discuss in full detail ergodicity issues in the hybrid Monte Carlo (HMC) (Appendix A), analytical solutions for individual instantons with emphasis on the topological winding number interpretation of the instanton (Appendix B), Hessians for N-instanton saddle points (Appendix C), details of the grand-canonical Monte Carlo (GCMC) simulation for the classical instanton model (Appendix D), and, finally, the relation of the instanton to the Gutzwiller projection (Appendix E).

II. BACKGROUND

This paper builds on previous work [12] which employed methods from lattice gauge theories to elucidate the physics of the Hubbard model, both at half filling and at finite density. The aim of this section is to recall the basic definitions and setup to motivate the study of the saddle points and understand the physics which they encode. This will motivate the formulation of an instanton gas model which captures much of the physics of the Hubbard model.

A. Hubbard model

In this paper, the Hubbard model on a bipartite (square and hexagonal) lattice is considered. The SU(2)-spin symmetric form of the Hamiltonian is given by

$$\hat{H} = -\kappa \sum_{\langle \boldsymbol{x},\boldsymbol{y}\rangle} (\hat{a}_{\boldsymbol{x}}^\dagger \hat{a}_{\boldsymbol{y}} + \hat{b}_{\boldsymbol{x}}^\dagger \hat{b}_{\boldsymbol{y}} + \text{H.c.}) + \frac{U}{2}\sum_{\boldsymbol{x}} \hat{q}_{\boldsymbol{x}}^2 + \mu \sum_{\boldsymbol{x}} \hat{q}_{\boldsymbol{x}}, \tag{1}$$

where $\hat{a}_{\boldsymbol{x}}^\dagger$ and $\hat{b}_{\boldsymbol{x}}^\dagger$ are creation operators for electrons and holes, obtained from the creation-annihilation operators for spin-up and spin-down electrons ($\hat{c}_{\boldsymbol{x},\sigma}$, $\hat{c}_{\boldsymbol{x},\sigma}^\dagger$, $\sigma = \uparrow, \downarrow$) via standard substitution,

$$\hat{a}_{\boldsymbol{x}}^\dagger = \hat{c}_{\boldsymbol{x},\uparrow}^\dagger, \quad \hat{b}_{\boldsymbol{x}}^\dagger = \pm \hat{c}_{\boldsymbol{x},\downarrow}, \tag{2}$$

where the sign in the second equation alternates depending on sublattice. The charge operator is introduced via the relation $\hat{q}_{\boldsymbol{x}} = \hat{n}_{\boldsymbol{x},\text{el}} - \hat{n}_{\boldsymbol{x},\text{h}} = \hat{a}_{\boldsymbol{x}}^\dagger \hat{a}_{\boldsymbol{x}} - \hat{b}_{\boldsymbol{x}}^\dagger \hat{b}_{\boldsymbol{x}}$, κ is the hopping parameter, $U > 0$ is the Hubbard interaction, and μ is the chemical potential. From now on, we will express all dimensional parameters like U, inverse temperature β, etc., in the units of hopping κ. This form of the Hamiltonian will be useful for the functional integral approach where the interaction term will be decomposed by the introduction of an auxiliary bosonic field. Away from half filling, $\mu = 0$, the theory suffers from the notorious sign problem. This is a generic feature of a large class of many-body theories and to deal with this problem, a variety of different methods and techniques have been devised [11,24–32]. The case of finite chemical potential will only briefly be commented on, while the case of half filling will be the main focus in all subsequent numerical and analytical calculations.

At half filling, this model is known to exhibit a semimetal-to-insulator transition ([22,23]). At large U, the Hubbard model on the hexagonal lattice exhibits AFM order while at small U it is a Dirac semimetal with no long-range order. The critical coupling, U_c, at which this transition takes place, defines an appropriate physical scale for the interaction strength. In the functional integral approach, not only can one take into account all quantum fluctuations which accurately describe both phases, but one can also employ semiclassical methods. These methods rely on knowledge of the stationary points of the action and fluctuations around the solutions to these saddle-point equations. One, in principle, could ask how the character and importance of these saddle-point solutions vary as the system passes through the phase transition. This is one of the questions we have addressed in this paper.

B. Path integral formulation

This study involves the path integral formulation of the Hubbard model. Previous studies have detailed this construction [19,33], which we briefly review here. The approach starts with the standard expression for the partition function as the trace of the quantum Boltzmann weight:

$$\mathcal{Z} = \text{Tr}\,(e^{-\beta\hat{H}}). \tag{3}$$

Denoting the hopping term in Eq. (1) as $\hat{H}_0$ and the Hubbard term as $\hat{H}_U$, one performs the following Trotter decomposition of the Boltzmann weight Eq. (3):

$$\text{Tr}\,(e^{-\beta\hat{H}}) = \text{Tr}\,(e^{-\Delta\tau\hat{H}_0} e^{-\Delta\tau\hat{H}_U})^{N_\tau} + O(\Delta\tau^2), \tag{4}$$

where the Euclidean time step $\Delta\tau \equiv \beta/N_\tau$ has been introduced and on the right-hand side of Eq. (4) there are N_τ repetitions of the exponential factors involving the kinetic and the Hubbard terms. In turn, $2N_\tau$ Grassmann resolutions of the identity are introduced, one between each exponential factor, and the matrix elements of the exponential factors are then computed. This is straightforward for the kinetic term, since $\hat{H}_0$ is bilinear in the fermionic operators. To deal with the four-fermion interaction term, continuous auxiliary bosonic fields are introduced at each Euclidean time slice through the usual Gaussian HS transformation:

$$e^{-\frac{\Delta\tau}{2}U\hat{q}_{\boldsymbol{x}}^2} \cong \int d\phi_{\boldsymbol{x}} e^{-\frac{\phi_{\boldsymbol{x}}^2}{2U\Delta\tau} + i\phi_{\boldsymbol{x}}\hat{q}_{\boldsymbol{x}}}. \tag{5}$$

After applying this to each factor of $e^{-\Delta\tau\hat{H}_U}$ in the Trotterized Boltzmann factor and integrating out the Grassmann variables, one obtains the following expression for the functional integral:

$$\mathcal{Z} = \int \mathcal{D}\phi e^{-S_B[\phi]} \det M_{\text{el}}[\phi] \det M_{\text{h}}[\phi],$$
$$S_B[\phi] = \sum_{\boldsymbol{x},\tau} \frac{\phi_{\boldsymbol{x},\tau}^2}{2U\Delta\tau}, \tag{6}$$

where M_{el} and M_{h} are the fermionic operators for the electrons and holes, respectively. The determinants of these operators can conveniently be expressed as

$$\det M_{\text{el}} = \det\left[I + \prod_{\tau=1}^{N_\tau} D_{2\tau-1} D_{2\tau}\right],$$
$$\det M_{\text{h}} = \det\left[I + \prod_{\tau=1}^{N_\tau} D_{2\tau-1} D_{2\tau}^*\right], \tag{7}$$

where $D_{2\tau} \equiv \text{diag}\,(e^{i\phi_{\boldsymbol{x},\tau}})$ and $D_{2\tau+1} \equiv e^{-\Delta\tau h}$ have been introduced. Both of these are $N_S \times N_S$ matrices, where N_S is the total number of spatial lattice sites. We have also introduced h, which is the matrix characterizing the tight-binding Hamiltonian $\hat{H}_0$. From the form of the determinants in Eq. (7), one can show that the integrand of the functional integral Eq. (6) is real and positive-definite at half-filling since $\det M_{\text{el}} = \det M_{\text{h}}^*$.

C. Lefschetz thimbles and the gradient flow

To construct an effective theory based on a semiclassical approach to the path integral for the repulsive Hubbard model on both the hexagonal and square lattices, one must first quantitatively understand the saddle points of the theory. The Lefschetz thimble decomposition of the partition function serves as the mathematical basis for a precise study of these saddle points. The idea of the Lefschetz thimbles approach is to complexify the space of fields over which we integrate in the functional integral. It is especially useful when the action is complex and its oscillatory phase precludes the use of importance sampling methods. Picard-Lefschetz theory, a generalization of Morse theory to complex manifolds, provides a framework by which this poorly behaved integral is converted into a sum of strictly convergent integrals. Considering the most general form of the functional integral for a generic lattice theory with N bosonic fields, one can write [8,9]

$$\mathcal{Z} = \int_{\mathbb{R}^N} \mathcal{D}\Phi\, e^{-S[\Phi]} = \sum_\sigma k_\sigma \mathcal{Z}_\sigma,$$
$$\text{where} \quad \mathcal{Z}_\sigma = \int_{\mathcal{I}_\sigma} \mathcal{D}\Phi\, e^{-S[\Phi]}, \tag{8}$$

and σ labels all complex saddle points $z_\sigma \in \mathbb{C}^N$ of the action. Here $\mathcal{I}_\sigma$ are the thimble manifolds attached to the saddle points. These manifolds, defined below, are the generalization of the contours of steepest descent in the theory of asymptotic expansions. This is what is known as the Lefschetz thimble decomposition of the functional integral. The saddle points are determined by the condition

$$\left.\frac{\partial S}{\partial \Phi}\right|_{\Phi = z_\sigma} = 0, \tag{9}$$

while the integer-valued coefficients k_σ encode the intersection of a manifold which we call the antithimble with the original domain of integration. At half filling, all saddles lie in the original, real space of fields. We stress here that if the saddle points are nondegenerate ($\det \partial^2 S/\partial\Phi'\partial\Phi|_{\Phi=z_\sigma} \neq 0$) and isolated, the relation Eq. (8) holds (for a generalization to the case of gauge theory see Ref. [9]).

The Lefschetz thimble is a manifold associated with a given saddle point. Let us endow the fields with an additional, nonphysical temporal parameter t, and define the gradient flow (GF) equation as

$$\frac{d\Phi}{dt} = \overline{\frac{\partial S}{\partial \Phi}}, \tag{10}$$

where the bar denotes complex conjugation. The Lefschetz thimble is the union of all fields $\Phi(t=0)$ that satisfy the boundary condition: $\Phi(t=0) \in \mathcal{I}_\sigma$ if $\Phi(t \to -\infty) \to z_\sigma$. Just as we have made an analogy between the thimble and the contour of steepest ascent, there is a second manifold associated with each saddle point which is analogous to the contour of steepest descent. This manifold is known as the antithimble, $\mathcal{K}_\sigma$, and consists of all possible $\Phi(t=0)$ which end up at a given saddle point z_σ: $\Phi(t=0) \in \mathcal{K}_\sigma$ if $\Phi(t \to +\infty) \to z_\sigma$. As previously stated, k_σ counts the number of intersections of $\mathcal{K}_\sigma$ with $\mathbb{R}^N$, $k_\sigma = \langle \mathcal{K}_\sigma, \mathbb{R}^N \rangle$. Along a given thimble, the imaginary part of the action is constant, and thus one can rewrite the Lefschetz decomposition of the functional integral as

$$\mathcal{Z} = \sum_\sigma k_\sigma e^{-i \operatorname{Im} S} \int_{\mathcal{I}_\sigma} \mathcal{D}\Phi\, e^{-\operatorname{Re} S[\Phi]}, \tag{11}$$

which makes the previously mentioned claim of converting an oscillatory integral to a sum of convergent ones abundantly clear. Early success with this method centered around the study of toy models without fermions. Recently, however, it has been used to address the sign problem in both nontrivial, low-dimensional relativistic field theories [24,29,31] as well as in two-dimensional many-body systems [32,34].

As evident from Eq. (11), the application of the thimble decomposition would be much easier if one knew the structure of the saddle points, z_σ, in advance. In this case, it would be possible to simplify Eq. (11) by considering only the dominant saddles or by using the Gaussian approximation to the integrals. The instanton gas approach performs exactly this task: it predicts the dominant saddle for the Hubbard model for a wide range of parameters without prior QMC simulations.

III. STRUCTURE OF THE SADDLE POINTS FROM QMC DATA

In previous studies [12], it was demonstrated how one can numerically determine the Lefschetz thimbles decomposition Eq. (8) at half filling, where the sign problem is absent and all thimbles are confined to the real subspace $\mathbb{R}^N$. We first generate configurations of the continuous bosonic auxiliary fields according to their weight e^{-S}, where

$$S = S_B - \ln(\det M_{\text{el}} \det M_{\text{h}}). \tag{12}$$

In the next stage, we evolve the auxiliary fields according to the GF equations in the inverse direction,

$$\frac{d\Phi}{dt} = -\frac{\partial S}{\partial \Phi}, \tag{13}$$

starting from each of these QMC-generated field configurations. These flows converge to the local minima of the action within $\mathbb{R}^N$, which are, of course, just the relevant saddle points. At the end of such a procedure, we obtain a set of saddle-point field configurations, distributed according to their relative weight in the full partition function: $\mathcal{Z}_\sigma/\mathcal{Z}$. This distribution can be plotted as the histogram of the actions of these various saddle-point field configurations. The technical details of this procedure as well as some additional checks (e.g., the question of ergodicity of QMC generator and the continuum limit) can be found in Appendix A.

In general, the number and the form of the saddle-point configurations critically depend on the way in which we introduce the auxiliary fields [12]. In this paper, we are interested in an analytical saddle-point approximation. Thus, we employ the specific HS decomposition, where the scalar auxiliary field ϕ is coupled to the charge density. In this particular case, the saddle points are especially simple, as their histogram can be seen to be a collection of equidistant discrete peaks, as clearly displayed in Fig. 4. This regular saddle structure makes the creation of an analytical saddle-point approximation relatively straightforward.

A. Individual instantons

The discrete structure of the histograms which characterize the values of the action of the saddle points has a particularly simple explanation. As was already shown in our previous work [12], all nonvacuum saddle points for this particular choice of the HS transformation Eq. (5) are formed by a collection of individual localized field configurations. For convenience, we repeat here the plot, showing this type of configuration for the auxiliary bosonic field (Fig. 5). One can clearly see that $\phi_{\boldsymbol{x},\tau}$ is localized both in Euclidean time and in space. This field configuration is the solution for the Euclidean

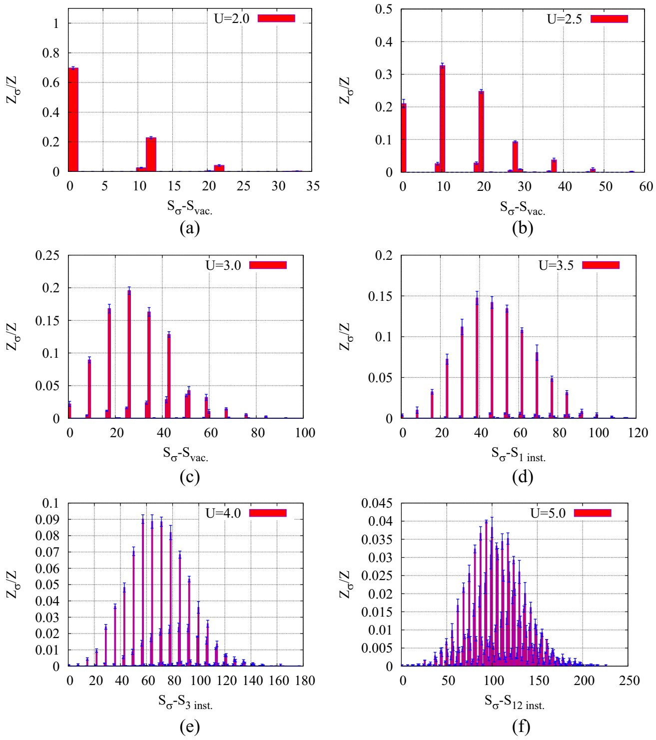

(a) (b)

(c) (d)

(e) (f)

FIG. 4. Histograms depicting the relative contributions of the various N-instanton saddles to the full partition function. The horizontal axis corresponds to the action of an N-instanton solution, offset by an amount equal to the action of the observed saddle with the least number of instantons. One can clearly see that the minimal number of observed instantons increases with increasing U. These calculations were performed on a 6×6 lattice with $N_\tau = 512$, $\beta\kappa = 20$.

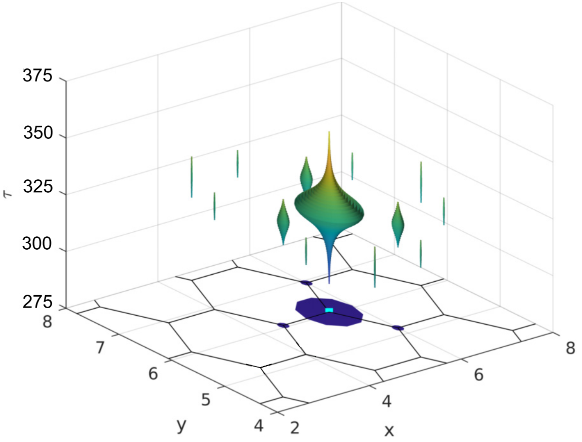

FIG. 5. Visualization of the $\phi_{x,\tau}$ field for the saddle-point configuration with one instanton. The widths of the vertical spindles correspond to the value of $|\phi_{x,\tau}|$ at a given spatial lattice site and time step in Euclidean time. For clarity, we only draw the spindles if $|\phi_{x,\tau}| > \epsilon$, where ϵ is some suitably small threshold. To clearly illustrate the spatial positions of the spindles within the lattice, we also draw their projections on the $\tau = 275$ plane. Calculations were carried out on a 6×6 lattice with interaction strength $U = 5.0\kappa$, $N_\tau = 512$, and $\beta\kappa = 20$.

equations of motions for the auxiliary field $\phi_{\boldsymbol{x},\tau}$ following from the action Eq. (12). We will henceforth refer to this field configuration as an *instanton*. The detailed reasons for this are outlined in Appendix B. The one subtlety is that we should take into account the back reaction from the fermionic determinant from the very beginning, as the bosonic part of the action Eq. (6) is purely Gaussian. Each instanton is defined by its location in space (including sublattice), position of its center (where $|\phi_{\boldsymbol{x},\tau}|$ is largest) in Euclidean time, and the binary instanton-anti-instanton index. The instanton-anti-instanton index reflects the symmetry of the integrand in Eq. (5) with respect to the sign of the auxiliary bosonic field. Thus, the anti-instanton configuration is related to the instanton by simply inverting the sign of the auxiliary field at each spatial lattice site and on all time slices, $\phi_{\boldsymbol{x},\tau} \to -\phi_{\boldsymbol{x},\tau}$.

With this information at hand, the histograms in Fig. 4 can be easily understood: the first bar, at $S_\sigma = S_{\text{vac}}$, corresponds to the vacuum field configuration ($\phi_{\boldsymbol{x},\tau} = 0$); the next bar, at $S^{(1)}$, is the saddle with just one instanton located at a random position inside the lattice, which is allowed by translational symmetry; the third bar, at $S^{(2)}$, corresponds to the saddle with two instantons, etc. The width of the bars does not substantially increase as the number of instantons increases, which means that the action of the $N-$instanton field configuration is still approximately equal to $S^{(N)} = S_{\text{vac}} + N(S^{(1)} - S_{\text{vac}})$. Thus, the action of the N-instanton configurations is only weakly dependent on the relative position of the instantons, at least if the density of instantons is not too large. Therefore, we can effectively describe the saddle points as a gas of weakly interacting instantons. This conjecture is further supported by the data shown in Fig. 6. This plot clearly illustrates that the weight of the one-instanton saddle is proportional to both the spatial size of the lattice and the inverse temperature,

$$\mathcal{Z}_1/\mathcal{Z} \sim N_S\beta, \tag{14}$$

where $\mathcal{Z}_1$ is the sector of the partition function, corresponding to the integral over the thimble attached to the one-instanton saddle. Thus, the localized one-instanton field configuration is not sensitive to the lattice size, provided that its dimensions exceed the size of the instanton.

The next step is the study of N-instanton saddles and the interaction of instantons. However, before we turn to the instanton interaction, a few words are in order concerning the continuum limit. Unlike the case of relativistic lattice field theories, the limit of zero lattice spacing is only to be taken for the Euclidean time direction. This is needed to be sure that the error introduced in our Trotter decomposition of the Boltzmann weight can be neglected. As we can see from the analysis in Appendix A, the weights of the $N-$instanton saddles are independent of the lattice spacing in Euclidean time, and thus our numerical results are already effectively at the continuum limit. This property should also be a requirement of the analytical saddle point approximation. However, a certain complication stems from the fact that the saddles, like the one shown in Fig. 5, are degenerate with respect to the continuum symmetry of translations in Euclidean time. Instead of a single saddle, we in fact have a closed valley in configuration space and it appears that the minimal approximation which has a well-defined continuum limit is the Gaussian integral in

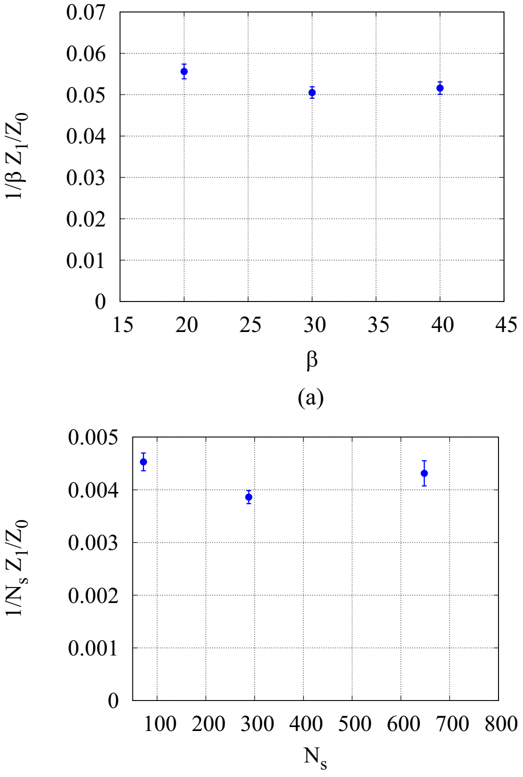

(a)

(b)

FIG. 6. (a) The relative weight of the first nonvacuum thimble with respect to the full partition function as a function of the inverse temperature. The calculations were carried out on a 6×6 lattice, with a Euclidean time step corresponding to $N_\tau = 512$ at $\beta\kappa = 20$. (b) The scaling of the relative weight of the first nonvacuum thimble with the spatial system size at fixed $\beta\kappa = 20$ and $N_\tau = 512$. The interaction strength is fixed at $U = 2.0\kappa$ for all plots.

all directions except that of the zero mode associated with the translational symmetry in Euclidean time.

The removal of the zero mode taking into account the collective coordinate factor is well-known in the instanton calculus (see, e.g., Refs. [14,35]). For the sake of completeness, we nevertheless consider here explicitly the analytic expression for the partition function in the one-instanton sector in Gaussian approximation. Let $\phi^{(X,T)}_{\boldsymbol{x},\tau}$ be the one-instanton configuration centered at the space time point (X, T), where the coordinate $X = (\nu, \boldsymbol{r})$ includes the spatial position of the center of the instanton $\boldsymbol{r}$ (including the sublattice index) and the binary instanton-anti-instanton index $\nu = \pm 1$, while the Euclidean time position is denoted by $T \in [0; \beta)$. All these configurations belong to one valley $O^{(1)} = \bigcup_{T\in[0;\beta)} \phi^{(X,T)}$, with the instanton center T being its parameter:

$$\left.\frac{\partial S(\phi)}{\partial \phi_{\boldsymbol{x},\tau}}\right|_{\phi=\phi^{(X,T)}, T\in[0;\beta)} = 0. \tag{15}$$

We now approximate the action by considering Gaussian fluctuations of the field around the saddle

$$\begin{aligned} S \approx S(\phi^{(X,T)}) &+ \tfrac{1}{2}\big(\phi_{\boldsymbol{x},\tau_1} - \phi^{(X,T)}_{\boldsymbol{x},\tau_1}\big) \\ &\times \mathcal{H}^{(1)}_{(\boldsymbol{x},\tau_1),(\boldsymbol{y},\tau_2)}\big(\phi_{\boldsymbol{y},\tau_2} - \phi^{(X,T)}_{\boldsymbol{y},\tau_2}\big), \end{aligned} \tag{16}$$

where

$$\mathcal{H}^{(1)}_{(\boldsymbol{x},\tau_1),(\boldsymbol{y},\tau_2)} = \left.\frac{\partial^2 S(\phi)}{\partial \phi_{\boldsymbol{x},\tau_1}\partial \phi_{\boldsymbol{y},\tau_2}}\right|_{\phi=\phi^{(X,T)}} \tag{17}$$

is the Hessian of the one-instanton saddle point. We denote the eigenvalues of $\mathcal{H}^{(1)}$ as $\lambda^{(1)}_i$, $i = 0 \ldots N_S - 1$. This set contains the zero mode, $\lambda^{(1)}_0 = 0$, due to the above-mentioned translational symmetry.

Now, $\mathcal{Z}_1$ can be written as the line integral along the curve $O^{(1)}$ in configuration space:

$$\mathcal{Z}_1 = 2N_S \int_{O^{(1)}} d\tilde{\phi}_0 \mathcal{Z}^P_1(\{\phi^{(X,T)}\}), \tag{18}$$

where the $2N_S$ factor describes the trivial discrete spatial and instanton-anti-instanton degeneracies and $\mathcal{Z}^P_1$ is what we will refer to as the partial partition function. Here we have introduced $d\tilde{\phi}_0$, which is the differential arc length of the $O^{(1)}$ curve,

$$d\tilde{\phi}_0 = \big|\big|\phi^{(X,T+dT)} - \phi^{(X,T)}\big|\big|, \tag{19}$$

such that the length of the valley is

$$L^{(1)} = \int_0^\beta dT \left|\left|\frac{\phi^{(X,T+dT)} - \phi^{(X,T)}}{dT}\right|\right|. \tag{20}$$

In practice, $L^{(1)}$ on the lattice is the collection of N_τ steps, each corresponding to the shift $T \to T + \Delta\tau$. Thus, according to Eq. (20), $L^{(1)}$ can be approximated by the following finite difference of field values:

$$L^{(1)} = N_\tau \sqrt{\sum_{\boldsymbol{x},\tau} \big(\phi^{(X,0)}_{\boldsymbol{x},\tau} - \phi^{(X,\Delta\tau)}_{\boldsymbol{x},\tau}\big)^2}. \tag{21}$$

Alternatively, we can take into account that the field configuration $\phi^{(X,T)}_{\boldsymbol{x},\tilde{\tau}}$ is in fact a function of the difference $\tilde{\tau} - T$, where the dimensional Euclidean time index: $\tilde{\tau} \in [0; \beta)$: $\tau = \tilde{\tau}/\Delta\tau$. Thus,

$$\frac{L^{(1)}}{\beta} = \big|\big|\Delta\phi^{(X,T)}\big|\big| = \sqrt{\sum_{\boldsymbol{x},\tau}\left(\frac{\phi^{(X,T)}_{\boldsymbol{x},\tau+1} - \phi^{(X,T)}_{\boldsymbol{x},\tau}}{\Delta\tau}\right)^2}, \tag{22}$$

where $||\Delta\phi^{(X,T)}||$ is the norm of the lattice derivative of the one-instanton field configuration with respect to the physical Euclidean time.

The partial partition function $\mathcal{Z}^P_1(\{\phi^{(X,T)}\})$ describes the Gaussian fluctuations around the configuration $\phi^{(X,T)}$ in all directions except the one corresponding to the zero mode:

$$\mathcal{Z}^P_1\big(\{\phi^{(X,T)}\}\big) = \int \prod_{i=1}^{N_S N_\tau - 1} d\tilde{\phi}_i e^{-S^{(1)} - \frac{1}{2}\sum_{i=1}^{N_S N_\tau - 1} \lambda^{(1)}_i \tilde{\phi}^2_i}. \tag{23}$$

Here, $\tilde{\phi}_i$ are the coordinates in configuration space in the directions of the corresponding eigenvectors of the Hessian $\mathcal{H}^{(1)}$, computed for the configuration $\phi^{(X,T)}$. Now, the eigenvalues of the Hessian $\lambda^{(1)}_i$ and the value of $\mathcal{Z}^P_1(\{\phi^{(X,T)}\})$ are in fact independent of the coordinates of the instanton center (X, T). This means that the integral Eq. (24) boils down to just

$$\begin{aligned} \mathcal{Z}_1 &= 2N_S \mathcal{Z}^P_1\big(\{\phi^{(X,T)}\}\big) \int_{O^{(1)}} d\tilde{\phi}_0 \\ &= 2N_S \mathcal{Z}^P_1\big(\{\phi^{(X,T)}\}\big) L^{(1)}. \end{aligned} \tag{24}$$

TABLE I. Here we display the valley lengths and Hessians for the one-instanton saddles on lattices of two different sizes in Euclidean time: $N_\tau = 256$ and $N_\tau = 512$. The remaining parameters are fixed with the spatial size given by 6×6 with $U = 2.0\kappa$, $\kappa\beta = 20$.

N_τ	$L^{(1)}$	$(\frac{\det \mathcal{H}_\perp^{(1)}}{\det \mathcal{H}^{(0)}})$	$\frac{\mathcal{Z}_1}{2N_S \mathcal{Z}_0}$
256	62.699	0.124533	445.398
512	44.272	0.06208	445.355

Performing the Gaussian integral in Eq. (23), the final expression for $\mathcal{Z}_1$ reads

$$\mathcal{Z}_1 = 2N_S L^{(1)} e^{-S^{(1)}} \sqrt{\frac{(2\pi)^{N_S N_\tau - 1}}{\prod_i' \lambda_i^{(1)}}}. \tag{25}$$

Here, the product of the eigenvalues of the Hessian in the denominator excludes the zero mode, for a total of $N_s N_\tau - 1$ eigenvalues. To reproduce the empirical relation given in Eq. (14), we restore physical units in Euclidean time according to Eq. (22) to obtain

$$\mathcal{Z}_1 = 2N_S \beta e^{-S^{(1)}} \left|\left|\Delta\phi^{(X,T)}\right|\right| \sqrt{\frac{(2\pi)^{N_S N_\tau - 1}}{\prod_i' \lambda_i^{(1)}}}. \tag{26}$$

If the inverse temperature β is substantially larger than the width of the instanton, the norm is independent of β and we reproduce the desired, empirically determined scaling in Eq. (14).

The absence of the zero mode in the product over eigenvalues in the denominator in Eq. (26) can be formally expressed as follows:

$$\det \mathcal{H}_\perp^{(1)} = \det\left(\mathcal{H}^{(1)} + \mathcal{P}^{(1)}\right) = \prod_{i=1}^{N_s N_\tau - 1} \lambda_i^{(1)}, \tag{27}$$

where $\det \mathcal{H}_\perp^{(1)}$ corresponds to the result of the Gaussian integral over all directions around the one-instanton saddle point excluding the zero mode, and $\mathcal{P}^{(1)}$ is the projection operator on to the zero mode direction in configuration space.

Finally, for the instanton structure of the partition function (for which the N-instanton saddle is dominant in $\mathcal{Z}$), we only need their ratio with respect to the part of the partition function corresponding to the vacuum saddle $\mathcal{Z}_N/\mathcal{Z}_0$. For the one-instanton saddle, this means that what we really need to compute is the following expression:

$$\frac{\mathcal{Z}_1}{\mathcal{Z}_0} = 2N_S L^{(1)} e^{-\tilde{S}^{(1)}} \left(2\pi \frac{\det \mathcal{H}_\perp^{(1)}}{\det \mathcal{H}^{(0)}}\right)^{-1/2}, \tag{28}$$

where $\tilde{S}^{(i)} = S^{(i)} - S_{\text{vac}}$. In this expression, $L^{(1)}$ is $\Delta\tau$ dependent and thus the Gaussian fluctuations in the perpendicular directions must be taken into account to achieve the $\Delta\tau$-independent results in the continuum limit. In this case, the $\Delta\tau$ dependencies in $L^{(1)}$ and in the Hessian matrices compensate each other. The numerical results for the expression in Eq. (28) are shown in Table I. The independence of $\tilde{S}^{(i)}$ on the step size in Euclidean time is shown in Appendix A. Evidently, our simulations are already close to the continuum limit, as the final result for the ratio $\mathcal{Z}_1/\mathcal{Z}_0$ is practically $\Delta\tau$ independent.

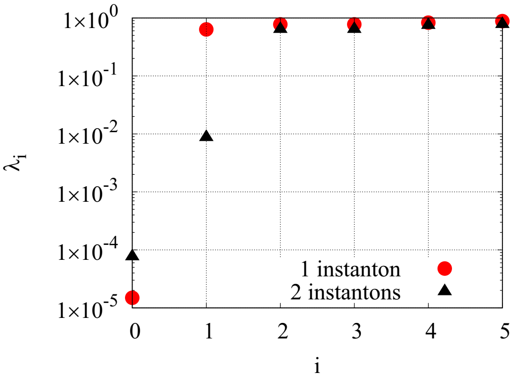

FIG. 7. The five lowest eigenvalues of the Hessian matrices computed at the one- and two-instanton saddle points. The calculations were performed on a 6×6 lattice with interaction strength $U = 6.0\kappa$, $N_\tau = 512$, and $\beta\kappa = 20$.

B. Interaction of instantons

In the previous section, we have described in detail the one-instanton saddle and its partition function. As the interaction U becomes large, it becomes increasingly likely for multi-instanton configurations to appear. While it may be appropriate in some regimes to treat these systems as a noninteracting gas of instantons, one would like to understand the interaction between instantons. In this section, we consider the two-instanton field configurations $\phi_{\boldsymbol{x},\tau}^{((X_1,T_1),(X_2,T_2))}$, where the coordinates (X_i, T_i), $i = 1, 2$ define the positions of the centers of the instantons.

The lowest eigenvalues of the Hessian for the one- and two-instanton saddles are shown in Fig. 7. Here, λ_0 corresponds to the zero mode (in actual numerical computations it is never exactly equal to zero due to the finite lattice spacing in Euclidean time). However, for the two-instanton saddle, we see that the next eigenvalue λ_1 is still much smaller then all λ_i for $i > 1$. This is what we refer to as a quasizero mode, which occurs due to the symmetry by which the instantons are shifted with respect to one another. Imagine two instantons with fixed spatial positions X_1 and X_2. Then, one can vary their time coordinates T_1 and T_2. The field configurations generated in this way form a two-dimensional torus in configuration space and the eigenvectors for λ_0 and λ_1 define tangent planes to this torus.

As was done in Eq. (26), we would like to construct an expression for the partition function of the two-instanton saddle. To faithfully represent the physics of the multi-instanton saddle, we must take into account the change of the action along the previously mentioned torus which defines the symmetry of the two-instanton saddle. At the same time, we must guarantee that our expression has a well-defined continuum limit in Euclidean time, $\Delta\tau \to 0$. This is encoded in the following expression:

$$\mathcal{Z}_2 = \frac{1}{2} \sum_{X_1, X_2} W^{(2)}(X_1, X_2), \tag{29}$$

where

$$W^{(2)}(X_1, X_2) = \int d\bar{T}\, d\Delta T e^{-S(X_1,X_2,\Delta T)} \sqrt{g(X_1, X_2, \Delta T)} \times \left(\prod_{i=2}^{N_S N_\tau - 1} \frac{2\pi}{\lambda_i(X_1, X_2, \Delta T)} \right)^{1/2}. \quad (30)$$

As in the case of the one-instanton saddle, both coordinates X_i include the spatial part with sublattice index and the binary instanton-anti-instanton index. The action of the field configuration, $S(X_1, X_2, \Delta T)$, is characterized by the two spatial locations and their separation in Euclidean time. The quantity $\sqrt{g}$ is the first fundamental form of the mapping of the surface of the two-dimensional torus to the center of mass and relative Euclidean time coordinates, $(\bar{T}, \Delta T)$, where

$$\bar{T} = \frac{T_1 + T_2}{2}, \quad (31)$$

$$\Delta T = T_1 - T_2. \quad (32)$$

Finally, the factor of $\frac{1}{2}$ in Eq. (29) compensates for the double counting, which appears due to the fact that the instantons are indistinguishable. Thus, after the exchange $X_1 \leftrightarrow X_2$ and $T_1 \leftrightarrow T_2$, we still arrive at the same saddle.

One can immediately notice that the integrand in Eq. (30) is independent of $\bar{T}$, as this direction corresponds to the true zero mode, where both instantons are simultaneously translated in the Euclidean time direction. We now can rewrite the integrand of the above expression in a suggestive way,

$$U^{(2)}(X_1, X_2, \Delta T) \equiv U_S^{(2)}(X_1, X_2, \Delta T) + U_g^{(2)}(X_1, X_2, \Delta T) + U_\lambda^{(2)}(X_1, X_2, \Delta T), \quad (33)$$

which we can identify as the two-body instanton interaction. The individual terms in Eq. (33) each have a clear interpretation and meaning. The first term represents the change in the action with respect to two, infinitely separated instantons:

$$U_S^{(2)}(X_1, X_2, \Delta T) = S(X_1, X_2, \Delta T) - S^{(2)}. \quad (34)$$

The next two terms come from re-exponentiating both the first fundamental form and the zero-mode regulated determinant of the Hessian matrix:

$$U_g^{(2)}(X_1, X_2, \Delta T) = -\tfrac{1}{2}(\ln g(X_1, X_2, \Delta T) - \ln g(X_1, X_2, \infty)), \quad (35)$$

$$U_\lambda^{(2)}(X_1, X_2, \Delta T) = \frac{1}{2} \sum_{i=2}^{N_S N_\tau - 1} (\ln \lambda_i(X_1, X_2, \Delta T) - \ln \lambda_i(X_1, X_2, \infty)). \quad (36)$$

$U_g^{(2)}$ is computed using the triangulation of the surface of a 2D torus formed by the field configurations of the two instanton solutions. All potentials are normalized by their values at infinitely large time separation between instantons. Together, these can be taken as the starting point for a many-body theory of pairwise-interacting semiclassical objects. The two-body instanton interaction can be investigated numerically. This is simply done, by hand, by combining two separate one-instanton configurations of the auxiliary bosonic field, where the instantons are located at two different lattice sites and separated by a fixed distance in Euclidean time. The bosonic term in the action, being Gaussian, is trivial, whereas the fermion determinant on a fixed background can be computed using the Schur complement solver [36]. Our findings are illustrated in Fig. 8. Here, several profiles of $U^{(2)}(X_1, X_2, \Delta T)$ for the instanton-instanton and instanton-anti-instanton pairs are plotted. As the instantons and anti-instantons are ultralocal

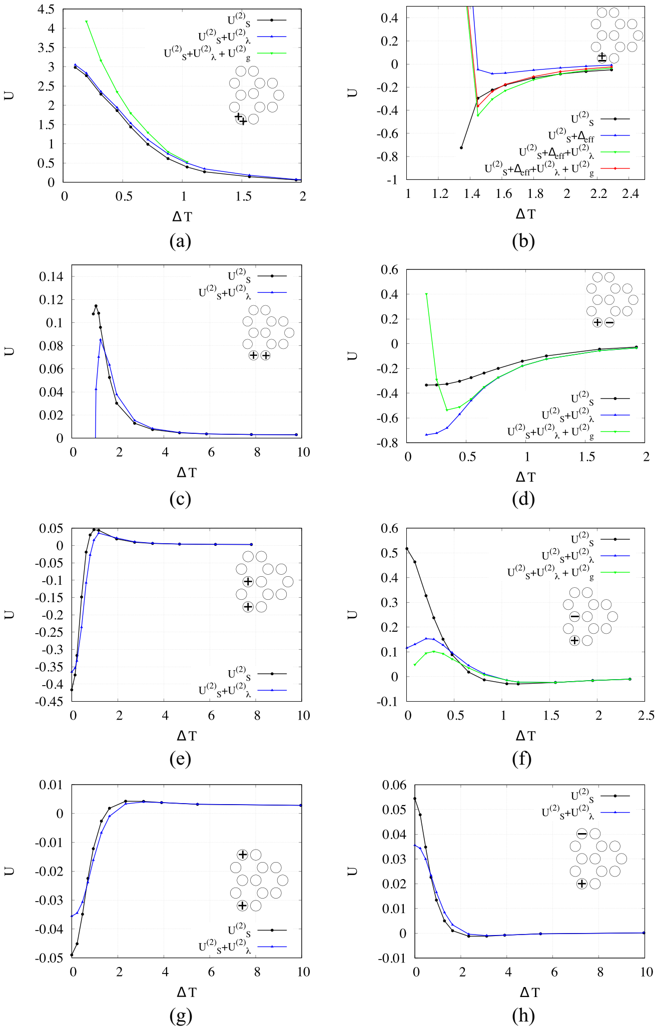

FIG. 8. The pairwise interaction of instantons and anti-instantons as a function of their separation in Euclidean time for a fixed spatial location. The plots in the left column [(a), (c), (e), (g)] correspond to interaction between a pair of instantons, while the plots in the right column [(b), (d), (f), (h)] correspond to the interaction between an instanton and an anti-instanton. The first row [(a), (b)] shows (anti)instantons at the same spatial lattice site, the second row [(c), (d)] corresponds to (anti)instantons located at nearest neighbors (opposite sublattices), the third row [(e), (f)] corresponds to a spatial separation of next-nearest neighbors, and the last row [(g, (h)] shows the interaction of (anti)instantons located at sites which are separated by two lattice unit vectors. In each case, we include a sketch of the corresponding spatial configuration on the hexagonal lattice in the inset. If $U_g^{(2)}$ is not shown, it means that its influence is small and the $U_S^{(2)} + U_\lambda^{(2)} + U_g^{(2)}$ line coincides with the $U_S^{(2)} + U_\lambda^{(2)}$ line. These calculations were performed on a 12×12 lattice with $\beta\kappa = 20$ and $N_\tau = 512$, with interaction strength $U = 4.6\kappa$.

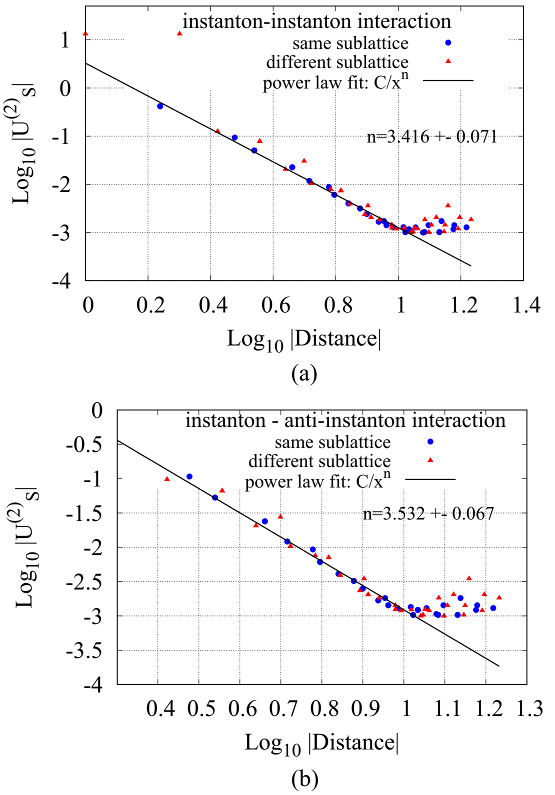

FIG. 9. (a) The action of an instanton-instanton pair as a function of the spatial separation between the instantons. In this case, zero action corresponds to the instantons being infinitely separated. (b) The same situation but for an instanton-anti-instanton pair. These calculations were performed on a 12×12 lattice with $\beta\kappa = 20$ and $N_\tau = 512$, and interaction strength $U = 4.6\kappa$. The (anti)instantons are placed at the same Euclidean time slice. The spatial separation is in units of the distance between nearest neighbors. In both cases, a power-law fit has been added.

in space (almost delta-function-like), only separations up to the distance of fourth-nearest neighbors on the hexagonal lattice are displayed. The two-body interaction rapidly decreases with increasing separation in Euclidean time as is visible from each of the plots in Fig. 8. For reference, the difference between the action of one instanton and the vacuum is equal to $\tilde{S}^{(1)} = 6.5658$ in this case. This means that, in general, the interaction strength is at least one order of magnitude smaller than the difference in action between the vacuum and a single instanton. Thus, we can treat instantons as noninteracting classical particles in 3D space, except for the case when they occupy the same spatial site. This is the so-called hard-core repulsion between instantons and anti-instantons which also appears in semiclassical models for the vacuum in QCD [37]. In addition to this, a noticeable effect is also a local, attractive interaction between an instanton and an anti-instanton on nearest-neighbor sites. The conclusion about the locality of the instanton-instanton interactions is further supported by the spatial profiles plotted in Fig. 9. In this case, we plot only the variation of the action $U_S^{(2)}(X_1, X_2, \Delta T = 0)$ and omit the other two terms. It is clearly shown to rapidly decrease with increased spatial separation. This implies that an ultralocal interaction accurately captures the physics of the saddle points.

However, there is a small caveat which we here note. Special treatment is needed when we consider the instanton and anti-instanton occupying the same spatial lattice site. In this case, they can actually annihilate, which means that the valley for the instanton-anti-instanton configuration is smoothly connected to the vacuum saddle:

$$\begin{cases} \tilde{X}_1 = (\nu, \boldsymbol{r}) \\ \tilde{X}_2 = (-\nu, \boldsymbol{r}) \end{cases} \Rightarrow S(\tilde{X}_1, \tilde{X}_2, \Delta T = 0) = S_{\text{vac}}. \qquad (37)$$

When constructing a semiclassical model of instantons and anti-instantons, a question naturally arises as to double counting. This is due to the fact that the vacuum saddle and Gaussian fluctuations around it were already taken into account by the factor $e^{-S_{\text{vac}}} \det \mathcal{H}^{(0)}$ in the approximate partition function. One way to address this issue of double counting is to consider the profile of the action and the corresponding probability distribution $e^{-S(\tilde{X}_1, \tilde{X}_2, \Delta T)}$ along the coordinate ΔT. If ΔT is small, we are close to the vacuum and the probability distribution for the field configurations can be written in Gaussian approximation as

$$P_{\text{vac}}^{\mathcal{H}}(\Delta T) = e^{-S_{\text{vac}} - \frac{1}{2}\mathcal{H}_{ij}^{(0)}\phi(\Delta T)_i \phi(\Delta T)_j}, \qquad (38)$$

where $\phi(\Delta T)_i$ is the field configuration for the instanton-anti-instanton pair at the same spatial lattice site x separated in Euclidean time by ΔT. For convenience, one can transform the lattice coordinates $(\boldsymbol{x}, \tau)$ into one-dimensional indices i and j via Eq. (C4). However, in reality, the probability distribution does not sharply vary with ΔT, since the action stabilizes around $S^{(2)}$. Thus, the distinction between this real probability distribution $e^{-S(\tilde{X}_1, \tilde{X}_2, \Delta T)}$ and $P_{\text{vac}}^{\mathcal{H}}$ is exactly the input needed from the instanton-anti-instanton saddle in the case of equal spatial coordinates. As a result, in the case of $X_1 = \tilde{X}_1$ and $X_2 = \tilde{X}_2$ [see Eq. (37)] we replace $S(X_1, X_2, \Delta T)$ with $S_{\text{eff}}(\tilde{X}_1, \tilde{X}_2, \Delta T)$ in Eq. (33), where $S_{\text{eff}}(\tilde{X}_1, \tilde{X}_2, \Delta T)$ is defined by the relation

$$e^{-S_{\text{eff}}} = e^{-S(\tilde{X}_1, \tilde{X}_2, \Delta T)} - P_{\text{vac}}^{\mathcal{H}}(\Delta T). \qquad (39)$$

It is convenient to write this in the form

$$S_{\text{eff}}(\tilde{X}_1, \tilde{X}_2, \Delta T) = S(\tilde{X}_1, \tilde{X}_2, \Delta T) + \Delta_{\text{eff}}(\Delta T), \qquad (40)$$

where we have introduced the following quantity:

$$\Delta_{\text{eff}}(\Delta T) = -\ln\left(1 - e^{-S(\tilde{X}_1, \tilde{X}_2, \Delta T) + S_{\text{vac}} + \frac{1}{2}\mathcal{H}_{ij}\phi(\Delta T)_i \phi(\Delta T)_j}\right). \qquad (41)$$

Results for this correction term are shown in the corresponding plot in Fig. 8(b), where the instanton and the anti-instanton reside at the same site of the hexagonal lattice (illustrated in the inset). As one would expect, its role rapidly decreases with increasing ΔT, since $S_{\text{eff}}(\tilde{X}_1, \tilde{X}_2, \Delta T)$ is almost indistinguishable from $S(\tilde{X}_1, \tilde{X}_2, \Delta T)$ in this limit. However, in the limit of small ΔT, the correction is extremely important. It forms a sharp repulsive barrier, which prevents the instanton and anti-instanton from annihilation, thus preventing the double counting of the vacuum saddle in the saddle-point decomposition.

In closing, we summarize the results of this section. The saddle points for the Hubbard model on the hexagonal lattice in the charge-density channel consist of individual localized field configurations: instantons and anti-instantons. These semiclassical objects form a weakly interacting gas in 3D (also taking into account the localization in Euclidean time). The only noticeable instanton-instanton or instanton-anti-instanton interaction is a strong repulsion when they occupy the same spatial lattice site and are closely separated in Euclidean time. This notion will be used in the next section for the construction of an analytical saddle-point approximation which will be used to reproduce the physics of the full theory as elucidated by our QMC calculations.

IV. INSTANTON GAS MODEL

Using analytical insights from Appendices B and C, as well as the numerical data described in the previous section, we can now switch to the construction of a weakly-interacting instanton gas model. First, we derive the approximate analytic expression for the free energy, only taking into account the hardcore repulsion in the instanton-instanton and instanton-anti-instanton pairs located at the same lattice site. As mentioned before, the minimal approximation, which supports the correct continuum limit $\Delta\tau = 0$, is the one which includes the Gaussian fluctuations around the saddle points. We propose that the partition function can be written as

$$\mathcal{Z} = \mathcal{Z}_0\left(1 + \sum_{k=1}^{\infty}\frac{\mathcal{Z}_k}{\mathcal{Z}_0}\right), \tag{42}$$

where $\mathcal{Z}_0$ is the vacuum partition function which corresponds to the Gaussian integral around the vacuum saddle point $\phi_{\boldsymbol{x},\tau} = 0$ and $\mathcal{Z}_k$ corresponds to the Gaussian integral around the $k-$instanton saddle point.

For the one-instanton saddle point, we take the ratio $\frac{\mathcal{Z}_1}{\mathcal{Z}_0}$ from Eq. (28). For the k-instanton saddle point, the weight within the Gaussian approximation can be computed using the results from Appendix C; namely, we use Eq. (C8) and neglect the variation of the first fundamental form $\sqrt{g}$ along the surface of the k torus formed by the saddle-point field configurations. One should also exclude the volume in Euclidean time and space, $\Delta\beta\mathcal{X}$, which is occupied by each instanton. Putting this all together, the final expression for the ratio $\frac{\mathcal{Z}_k}{\mathcal{Z}_0}$ takes the following form:

$$\frac{\mathcal{Z}_k}{\mathcal{Z}_0} = \frac{1}{k!}\left[\prod_{m=1}^{k}(\beta V - (m-1)\Delta\beta\mathcal{X})\right]2^{2k} \times e^{-k\tilde{S}^{(1)}}\left(\frac{L^{(1)}}{\beta}\right)^k\left(\frac{\det\mathcal{H}_\perp^{(1)}}{\det\mathcal{H}^{(0)}}\right)^{-k/2}\frac{1}{(2\pi)^{k/2}}, \tag{43}$$

where $V = N_S/2$ is the spatial volume of the lattice, and the sublattice index is taken into account in the 2^{2k} multiplier alongside the instanton-anti-instanton degeneracy. The multiplier $k!$ comes from the fact that the instantons are indistinguishable.

Formally, the sum over instanton sectors in Eq. (42) runs to infinity. However, in practice, we should truncate it at $k_{\max} = \lfloor\beta V/(\Delta\beta\mathcal{X})\rfloor$, when all free slots for instantons are taken. In other words, we stop at the point where the entire space-time volume is packed full of instantons. Under this assumption, the expression for the ratio $\frac{\mathcal{Z}}{\mathcal{Z}_0}$ can be summed exactly which yields the following expression:

$$\frac{\mathcal{Z}}{\mathcal{Z}_0} = 1 + \sum_{k=1}^{k_{\max}}\frac{k_{\max}!}{k!(k_{\max}-k)!}\gamma^k = (1+\gamma)^{k_{\max}}, \tag{44}$$

where we have introduced the quantity

$$\gamma \equiv \frac{4}{\sqrt{2\pi}}e^{-\tilde{S}^{(1)}}\left(\frac{\mathcal{X}\Delta\beta}{\beta}\right)L^{(1)}\left(\frac{\det\mathcal{H}_\perp^{(1)}}{\det\mathcal{H}^{(0)}}\right)^{-1/2}. \tag{45}$$

For practical calculations, we take $\mathcal{X} = 1$ and $\Delta\beta$ equal to the width of the instanton's profile (Fig. 5) at half height. Both the instanton profiles as well as the product $L^{(1)}(\frac{\det\mathcal{H}_\perp^{(1)}}{\det\mathcal{H}^{(0)}})^{1/2}$ are taken from the exact one-instanton saddle point.

Once we have the partition function for our gas of instantons, the free energy density can be computed as follows:

$$f - f_0 = -\frac{1}{\beta V}\ln\frac{\mathcal{Z}}{\mathcal{Z}_0}, \tag{46}$$

where

$$f_0 = -\frac{1}{\beta V}\ln\mathcal{Z}_0 \tag{47}$$

is the contribution to the free energy from the Gaussian integral around the vacuum saddle point. Using our previous results, we find

$$f = f_0 - \frac{1}{\Delta\beta\mathcal{X}}\ln(1+\gamma). \tag{48}$$

The physics described by the model has been reduced to the single parameter γ, which has temperature as well as coupling dependence.

Before further addressing the physics encoded in these expressions, we describe the predictions which can be made for the structure of the thimble decomposition from the analytical partition function. We are particularly interested in the possibility of predicting the structure of the dominant saddles which form the peaks in the distributions displayed in Fig. 4. Since each saddle can be characterized by the number of instantons, we can replot the distributions from Fig. 4 in terms of the number of instantons. This is done in Fig. 10 with an additional fit of the data to a Gaussian form. As one can see, the distributions can be quite precisely described by these curves, whereby only two parameters (the mean $\mathcal{C}$ and variance $\mathcal{D}$) are needed to characterize them. Another important effect which we observe is that the relative width of the distribution goes down with the increased system size. As one can see from the last plot in Fig. 10, the mean of the distribution scales as $\sim V$, but the width scales much more slowly. In fact, we will further show that the precise form of the scaling of the width with the volume is $\sim\sqrt{V}$. Thus, the distribution for the density of the instantons will approach a Dirac δ function in the thermodynamic limit. Therefore, in this limit, it suffices to consider only saddles where the number of instantons matches the mean value of the distribution.

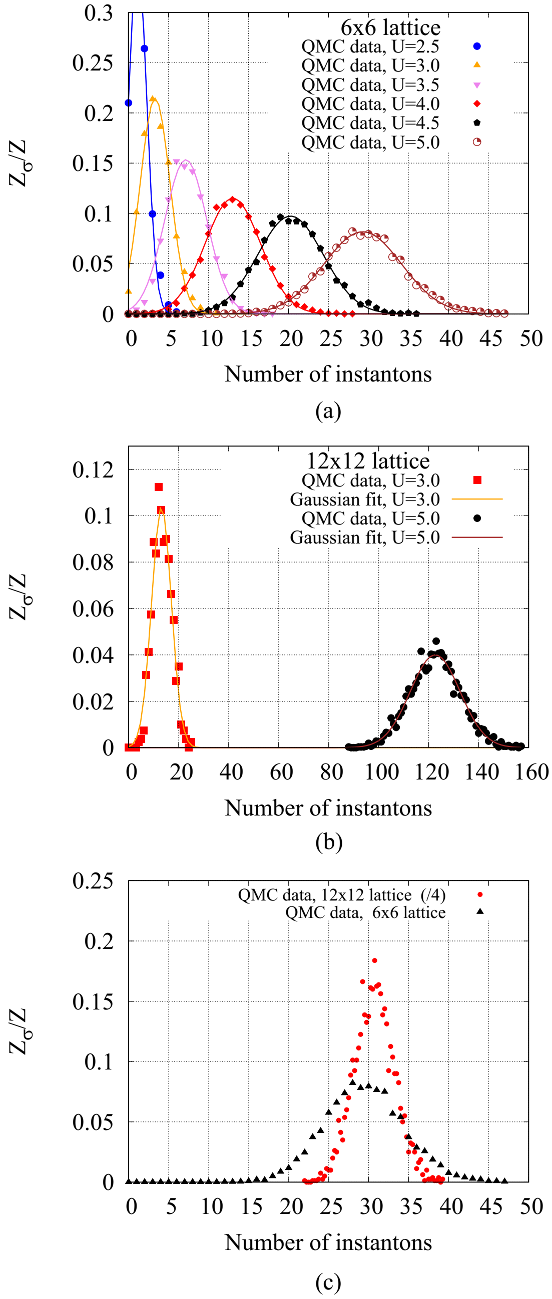

FIG. 10. The distribution of the number of instantons at various interaction strengths obtained from QMC configurations. The top two plots [(a), (b)] show the distributions obtained on 6×6 and 12×12 lattices, respectively, and the bottom plot (c) compares these data in the case of large interaction strength $U = 5.0\kappa$. We note that the x axis of the 12×12 lattice data is rescaled by a factor of 4 to have the curves lie on top of each other and to make the comparison more straightforward. All these calculations were performed at $\beta\kappa = 20$ and $N_\tau = 512$. For each data set, a Gaussian fit of the lattice data has also been performed—it is shown with the lines of the same colors as corresponding data sets.

The distribution of the number of instantons can be obtained from Eqs. (42)–(45) as $\mathcal{Z}_k/\mathcal{Z}$ in the limit $V \to \infty$ after we apply Stirling's approximation to the factorials in Eq. (44).

The final expressions for the mean of the distribution $\mathcal{C}$ and the variance $\mathcal{D}$ which follow from the instanton gas model are

$$\mathcal{C}_f = k_{\max}\frac{\gamma}{\gamma+1}, \tag{49}$$

$$\mathcal{D}_f = \sqrt{\frac{1}{\gamma+1}}. \tag{50}$$

From this, one sees that the physics of the saddles in the charge-density-coupled channel can be accurately described by the single parameter γ of our instanton gas model. As we will demonstrate further, despite its apparent simplicity, the model reproduces key features of the physics of the saddle decomposition of the Hubbard model on the hexagonal lattice.

Going further, it would be crucial to quantify the importance of interactions. Despite the relative smallness of interactions with respect to the action of a single semiclassical object, it is still worth checking whether they influence the characteristics of the final distribution of the instanton number. For this purpose, we construct a model of interacting instanton gas, where the pairwise interaction profiles are taken directly from our QMC data as described in Sec. II B. As the number of instantons is one of the thermodynamic variables of the system, it is necessary to work in the grand canonical ensemble. The microscopic state of the system is defined by the set of N coordinates for the individual instantons: $\{X_i, T_i\}$, $i = 1...N$. By generalizing Eqs. (29) and (30) to the case of an N-instanton saddle and taking into account only pairwise interactions, we arrive at the following grand canonical partition function for the interacting instanton gas:

$$\zeta = \sum_N \frac{1}{N!}\sum_{\{X_i\}}\int\prod_{i=1}^{N} dT_i\, e^{-\frac{1}{2}\sum_{i\neq j}^{N} U^{(2)}(X_i,X_j,T_i-T_j)+N\ln\tilde{\gamma}}, \tag{51}$$

where

$$\tilde{\gamma} \equiv \frac{1}{\sqrt{2\pi}}e^{-\tilde{S}^{(1)}}\frac{L^{(1)}}{\beta}\left(\frac{\det\mathcal{H}_{\perp}^{(1)}}{\det\mathcal{H}^{(0)}}\right)^{-1/2}. \tag{52}$$

As we did for the noninteracting instanton gas in Eq. (43), we only consider the ratios $\mathcal{Z}_k/\mathcal{Z}_0$. We recall that the pairwise interaction $U^{(2)}(X_i, X_j, T_i - T_j)$ is defined in Eq. (33). This model can be simulated using a classical GCMC, where the number of instantons N can be changed in the updates alongside with the coordinates (X_i, T_i) of the instantons already present in the system. The details of these calculations are described in Appendix D while below we discuss the important results of these classical simulations of the interacting instanton gas model.

A comparison of the predictions from the instanton gas model with the results from QMC for the structure of the thimbles decomposition is shown in Fig. 11. To compare the data for different lattice sizes in a uniform way, we plot the density of the instantons $\mathcal{C}/V$. To show that the variance scales as $\sqrt{V}$, we plot $\mathcal{D}/\sqrt{V}$ to demonstrate the collapse of the data obtained on different lattice volumes onto one curve. For the mean of the distribution, $\mathcal{C}$ (Fig. 10), we used the QMC data on 6×6 and 12×12 lattices to check that, indeed, the data from the full theory scales linearly with the volume. As we can see, both the analytical model Eq. (49) and the classical GCMC

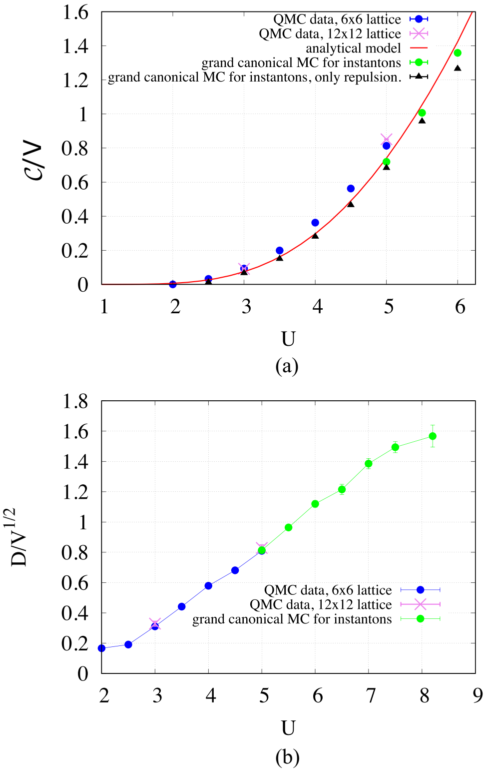

FIG. 11. (a) A comparison of the instanton density obtained from real QMC data with various instanton gas models. (b) The same comparison but for the variance. The QMC data corresponds to $N_\tau = 512$ and $\beta\kappa = 20$.

simulations which include pairwise interactions Eq. (51) yield a prediction for the mean of the distribution which is consistent with the one obtained in our QMC calculations. Thus, one could in principle predict the dominant thimble for a given set of lattice parameters (including lattice size, temperature, and interaction strength) even without doing actual QMC simulations, which are much more expensive.

Furthermore, the classical GCMC simulations of the instanton gas model Eq. (51) also provide an accurate prediction for the variance, as shown in Fig. 11(b). In particular, we obtain exactly the same results as QMC on a 6×6 lattice. In addition, the QMC data for a 12×12 lattice which has been rescaled by a factor of 2 exactly coincides with the data for the 6×6 lattice. This implies that unlike the mean $\mathcal{C}$, the variance $\mathcal{D}$ scales only as $\sim\sqrt{V}$. These two facts together show that, indeed, the distribution for the density of instantons, $\mathcal{C}/V$, tends to the δ function in thermodynamic limit. As the prediction from the analytical model in Eq. (50) was obtained exactly in the thermodynamic limit, $V \to \infty$, this model does not provide a good estimate for the variance on a finite lattice volume.

V. PHYSICS FROM THE INSTANTON GAS APPROXIMATION

In this section, we will concentrate on further physical predictions of the instanton gas model. First, we will consider the possibility to describe the semimetal to AFM phase transition, which is one of the most prominent features of the Hubbard model on the hexagonal lattice. Second, we consider the evolution of the electron density of states away from the Dirac point with increasing interaction strength.

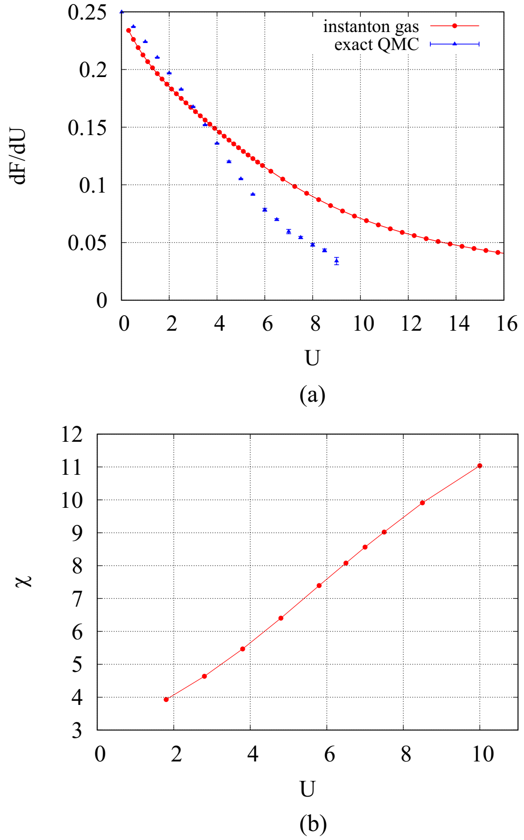

FIG. 12. (a) Double occupancy obtained from the instanton gas model and from QMC data. (b) AFM susceptibility obtained from the analytical model. In both cases, the instanton profiles and actions are obtained on the 6×6 lattice with $N_\tau = 512$ and $\beta\kappa = 20$ were used as input. QMC data were obtained on the same lattice.

A. Local magnetic fluctuations and long-ranged order

Starting from our simple expression for the free energy of the ensemble of instantons in Eq. (48), one can obtain further thermodynamic quantities by taking appropriate derivatives. In particular, the derivative of the free energy density, f, with respect to the Hubbard interaction gives us the double occupancy, which is defined as

$$\langle \hat{n}_{\mathbf{x},\uparrow} \hat{n}_{\mathbf{x},\downarrow} \rangle = \frac{\partial f}{\partial U}. \tag{53}$$

In practice, the derivative of the free energy over the interaction is computed by noting that γ is a function of U and taking the appropriate partials, $\partial_U \gamma$ and $\partial_U f_0$. The latter quantity can be directly obtained in the Gaussian approximation for $S_{\mathrm{vac}}(U)$, whereas $\det \mathcal{H}^{(0)}(U)$ can be computed numerically for a fixed spatial lattice size. The profiles for $\Delta\beta(U)$, $\tilde{S}^{(1)}(U)$, $L^{(1)}(U)$ and $\det \mathcal{H}_\perp^{(1)}(U)$ are obtained from the exact one-instanton field configurations we have obtained from our GF procedure discussed previously.

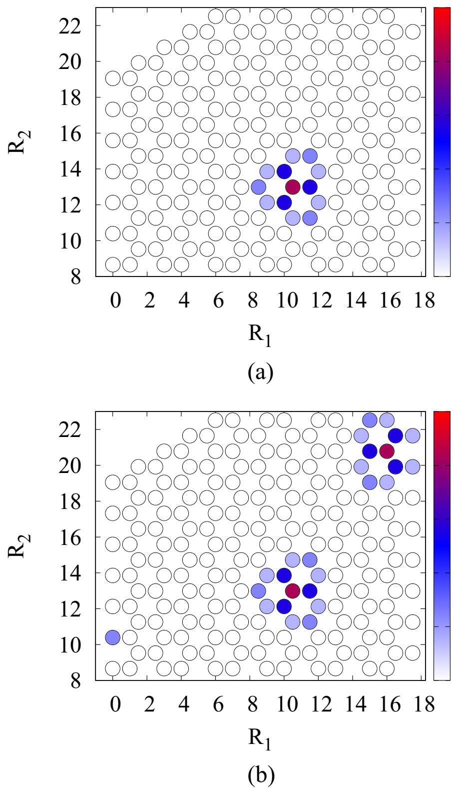

(a)

(b)

FIG. 13. The distribution of the squared spin across the hexagonal lattice for background field configuration consisting of a single instanton (a) or two instantons (b). What is plotted is the difference between the squared spin at a given lattice site x in the presence of semiclassical objects and its value for the vacuum configuration: $\langle\hat{S}_x^2\rangle|_{N_{\text{inst}}} - \langle\hat{S}_x^2\rangle|_{\text{vac}}$. A base-10 logarithmic scale is used for the color scale. Both instantons are located at the same Euclidean time slice where the spin operator is measured. This calculation refers to a 12×12 lattice with $\beta\kappa = 20$ and $N_\tau = 512$, with interaction strength $U = 2.0\kappa$. R_1 and R_2 are Cartesian coordinates of the lattice sites, displayed in the units of the distance between nearest neighbors.

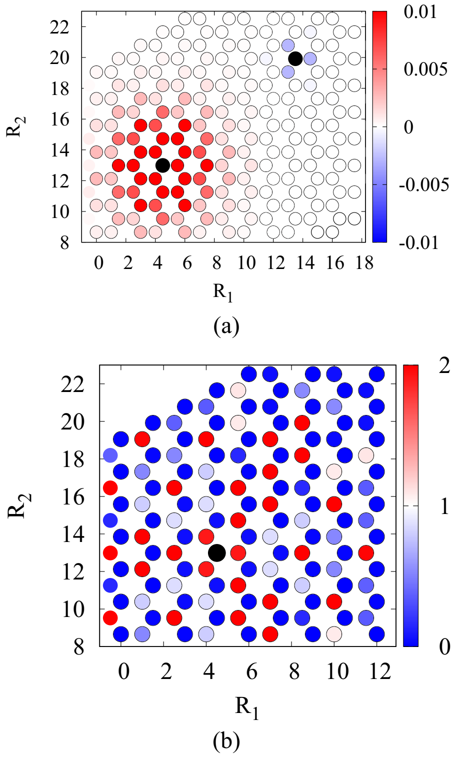

(a)

(b)

FIG. 14. (a) Charge-charge correlations, $\frac{1}{4}\langle\hat{q}_{\boldsymbol{x}_0}(T)\cdot\hat{q}_{\boldsymbol{x}_0+\boldsymbol{x}}(T)\rangle$, for a field configuration with one instanton at space-time (X, T). We consider two values of $\boldsymbol{x}_0$. The left black circle corresponds to $\boldsymbol{x}_0 = X$. The other value of $\boldsymbol{x}_0$ (right black circle) is far from the instanton. R_1 and R_2 are two Cartesian coordinates of the lattice sites, displayed in the units of the distance between nearest neighbors. The corresponding plot for the spin-spin fluctuations can be found in Fig. 1. (b) Ratio of spin-spin and charge-charge correlators on the same one-instanton saddle $4\langle\hat{S}^{(3)}_{\boldsymbol{x}_0}(T)\hat{S}^{(3)}_{\boldsymbol{x}_0+\boldsymbol{x}}(T)\rangle/\langle\hat{q}_{\boldsymbol{x}_0}(T)\hat{q}_{\boldsymbol{x}_0+\boldsymbol{x}}(T)\rangle$ centered at the location of the instanton $\boldsymbol{x}_0 = X$. The calculation was done on the same lattice as for Fig. 13(a).

The double occupancy as a function of interaction strength is plotted in Fig. 12(a). As one can see, we can successfully describe the increasing localization of electrons with increasing interaction strength. To understand how the reduction of the double occupancy comes about, we consider the local moment

$$\langle\hat{S}_{\boldsymbol{x}}^2\rangle - \langle\hat{S}_{\boldsymbol{x}}^2\rangle_{U=0} \equiv \frac{1}{4}\left[\frac{1}{2} - 2\langle\hat{n}_{\boldsymbol{x},\uparrow}\hat{n}_{\boldsymbol{x},\downarrow}\rangle\right] \tag{54}$$

at the saddle-point field configurations (Fig. 13). This quantity is computed using the fermionic propagator calculated at the saddle-point configuration of the auxiliary field. The distribution is shown both for the one- and two-instantons saddle points, where the centers of the instantons are located at the same time slice. As one can see, each instanton generates a localised region of excess spin, or reduced double occupancy, around the instanton center.

Figure 12(a) equally plots the double occupancy obtained with the Algorithm for Lattice Fermions [19] implementation of the finite-temperature auxiliary field QMC [20]. As in the instanton approach, local moment formation leads to a decrease of double occupancy. Owing to Eq. (53), we expect double occupancy to show nonanalytical behavior at the Gross-Neveu transition located at $U_c/\kappa \simeq 3.8$. The QMC data hints to nonanalytical behavior, whereas the instanton gas solution exhibits a very smooth curve. We will see below that this stems from the fact that the instanton approach does not capture the onset of the magnetic ordering and the resulting mass generation. We again note that the reduction of double occupancy is a dynamical effect that cannot be obtained at the mean-field level without breaking time-reversal symmetry [1,38].

Figure 14(a) shows the charge-charge $(\frac{1}{4}\langle\hat{q}_{\boldsymbol{x}}\hat{q}_{\boldsymbol{y}}\rangle)$ correlations at the one-instanton saddle, in the vicinity of the instanton and for reference away from it, where the correlator coincides with its vacuum values. The plot should be compared with the corresponding spin-spin correlator $\langle\hat{S}^{(3)}_{\boldsymbol{x}}\hat{S}^{(3)}_{\boldsymbol{y}}\rangle$ displayed in Fig. 1. The spin and charge correlators are equal in the vacuum. Both are zero if $\boldsymbol{x}$ and $\boldsymbol{y}$ are on the same sublattice and negative if $\boldsymbol{x}$ and $\boldsymbol{y}$ are at different sublattices. Around the instanton, both correlations are substantially enhanced, spin correlations remain AFM with the largest correlations still between points on different sublattices. The charge correlators change signs. The ratio $4\langle\hat{S}^{(3)}_{\boldsymbol{x}}\hat{S}^{(3)}_{\boldsymbol{y}}\rangle/\langle\hat{q}_{\boldsymbol{x}}\hat{q}_{\boldsymbol{y}}\rangle$ plotted in

Fig. 14(b) shows that the spin-spin correlations dominate over charge-charge correlations in the vicinity of the instanton. In particular, at lattice sites $\boldsymbol{x}$ and $\boldsymbol{y}$ that belong to different sublattices and where both spin-spin and charge-charge correlators acquire their largest values, spin correlations dominate. In summary, these figures demonstrate that the increased spin localization at the instanton core is surrounded by local AFM correlations. This key result is also shown in Fig. 1.

We next investigate long-range spin order characteristic of the AFM phase. The most obvious quantity to check is the spin susceptibility. It can be computed via the second derivative of the free energy with respect to an external, alternating magnetic field

$$\chi = \left.\frac{\partial^2 f}{\partial m^2}\right|_{m\to 0}, \tag{55}$$

where we introduced the explicit *staggered* mass term in the Hamiltonian Eq. (1):

$$\hat{H}_m = m\left(\sum_{x\in \text{1st sublat}} (\hat{n}_{x,\text{el}} + \hat{n}_{x,\text{h}}) - \sum_{x\in \text{2nd sublat}} (\hat{n}_{x,\text{el}} + \hat{n}_{x,\text{h}})\right). \tag{56}$$

This mass term contains the symmetry of the AFM ordering on the hexagonal lattice rewritten in terms of electrons and holes. Similarly to the calculation of the double occupancy Eq. (53), we compute the susceptibility using numerical derivatives of $S_{\text{vac}}(U,m)$, $\det \mathcal{H}^{(0)}(U,m)$, $\det \mathcal{H}^{(1)}_{\perp}(U,m)$, etc., with respect to the mass parameter m. These derivatives can be obtained from the corresponding one-instanton profiles at finite m after the application of the GF equations to the configurations generated in QMC simulations, in exactly the same manner as was done for $m=0$. This is possible due to the fact that the small staggered mass term does not alter the structure of the saddle points in the charge-coupled representation of the functional integral. The dependence of the susceptibility on the interaction strength is shown in Fig. 12(b). As is apparent, the susceptibility does not form a peak, signaling a phase transition but rather increases monotonically. Unfortunately, we can not extend our results much beyond $U = 10...15$, since the instantons become so densely packed that their interaction and the modification of their profiles due to mutual influence become really important. In this case, the approach similar to the instanton liquid model in QCD should be developed, which is beyond the scope of our paper. Taking into account these limitations, we conclude that the instanton gas approach captures local moment formation, but not the onset of long-ranged AFM ordering.

An additional argument in favor of the instanton as a path integral representation of a localized spin is presented in Appendix E, where we describe the technique which allows us to connect certain paths in the path integral to the properties of the ground-state wave function. Using this technique, we show that the ground state corresponding to the instanton is local Gutzwiller projection which suppresses the double occupancy at the site occupied by the instanton.

B. Single-particle spectral function

The spectral function of a single hole in an AFM defines a rich problem that has been extensively investigated with various methods. One expects the low-energy region to be captured by a spin polaron and a broad high energy spectral weight that is referred to as the upper Hubbard band [38–42]. Clearly, the instanton approach will not capture spin-polaron since there are no spin waves—Goldstone modes of the broken global symmetry—that will dress the doped hole. However, local magnetic fluctuations and the reduction of the double occupancy have the potential to account for the upper Hubbard band. It is very appealing to adopt a parton construction to account for the rich structure of the single-particle spectral function [43,44]. As an example, one can consider the orthogonal fermion representation of the Hubbard model [45,46]. Consider

$$\hat{H} = -t\sum_{\langle i,j\rangle,\sigma} \hat{f}^{\dagger}_{i,\sigma}\hat{f}_{j,\sigma}\hat{s}^{z}_{i}\hat{s}^{z}_{j} + \frac{U}{4}\sum_{i}\hat{s}^{x}_{i}, \tag{57}$$

where $\hat{f}^{\dagger}_{i,\sigma}$ is a fermion operator and $\hat{s}^{x,z}_{i}$, Pauli spin matrices acting on an Ising degree of freedom per site. The above defines a $\mathbb{Z}_2$ lattice gauge theory since

$$\hat{Q}_i = (-1)^{\hat{n}_i}\hat{s}^{x}_{i} \tag{58}$$

is a local conservation law. Here $\hat{n}_i = \sum_{\sigma}\hat{f}^{\dagger}_{i,\sigma}\hat{f}_{i,\sigma}$ and one will readily see that $\hat{Q}^2_i = 1$. Imposing the Gauss law,

$$\hat{Q}_i = 1. \tag{59}$$

Equation (57) reduces to the Hubbard model. The physical electron is a composite object,

$$\hat{c}^{\dagger}_{i,\sigma} = \hat{f}^{\dagger}_{i,\sigma}\hat{s}^{z}_{i}, \tag{60}$$

and using the Gauss law, we obtain

$$\hat{s}^{x}_{i} = (-1)^{\hat{n}_i} = 4(\hat{n}_{i,\uparrow} - 1/2)(\hat{n}_{i,\downarrow} - 1/2) \tag{61}$$

such that Eq. (57) maps precisely onto the Hubbard model. Within this framework, the low-energy spectral function accounts for the electron as described by a bound state of the f electron and an Ising spin. The high energy is a continuum where the composite object has *disintegrated*. We note that such a composite fermion interpretation of the single particle spectral function is equally appealing in the realm of heavy fermion systems [47,48]. We now compare the instanton approach to the auxiliary field QMC simulations, and will use the framework of the aforementioned parton picture to interpret the results. To produce the data for the instanton calculation, we first generate M sets of $N^{(r)}$ coordinates $\{X^{(r)}_k, T^{(r)}_k\}$ of instantons, where $r = 1...M$ and $k = 1...N^{(r)}$ using classical GCMC for the instanton gas model Eq. (51). The details of this approach are described in Appendix D. Using these coordinates for the instanton centers, we combine together the exact profiles of single instantons centered at these coordinates to get M saddle-point field configurations:

$$\phi^{(r)}_{\boldsymbol{x},\tau} = \sum_{k=1}^{N^{(r)}} \phi^{\left(X^{(r)}_k, T^{(r)}_k\right)}_{\boldsymbol{x},\tau}, \qquad r = 1...M. \tag{62}$$

In this expression, we do not take into account the change of the instanton profiles due to the overlap between different instantons. This approximation holds due to the relatively small

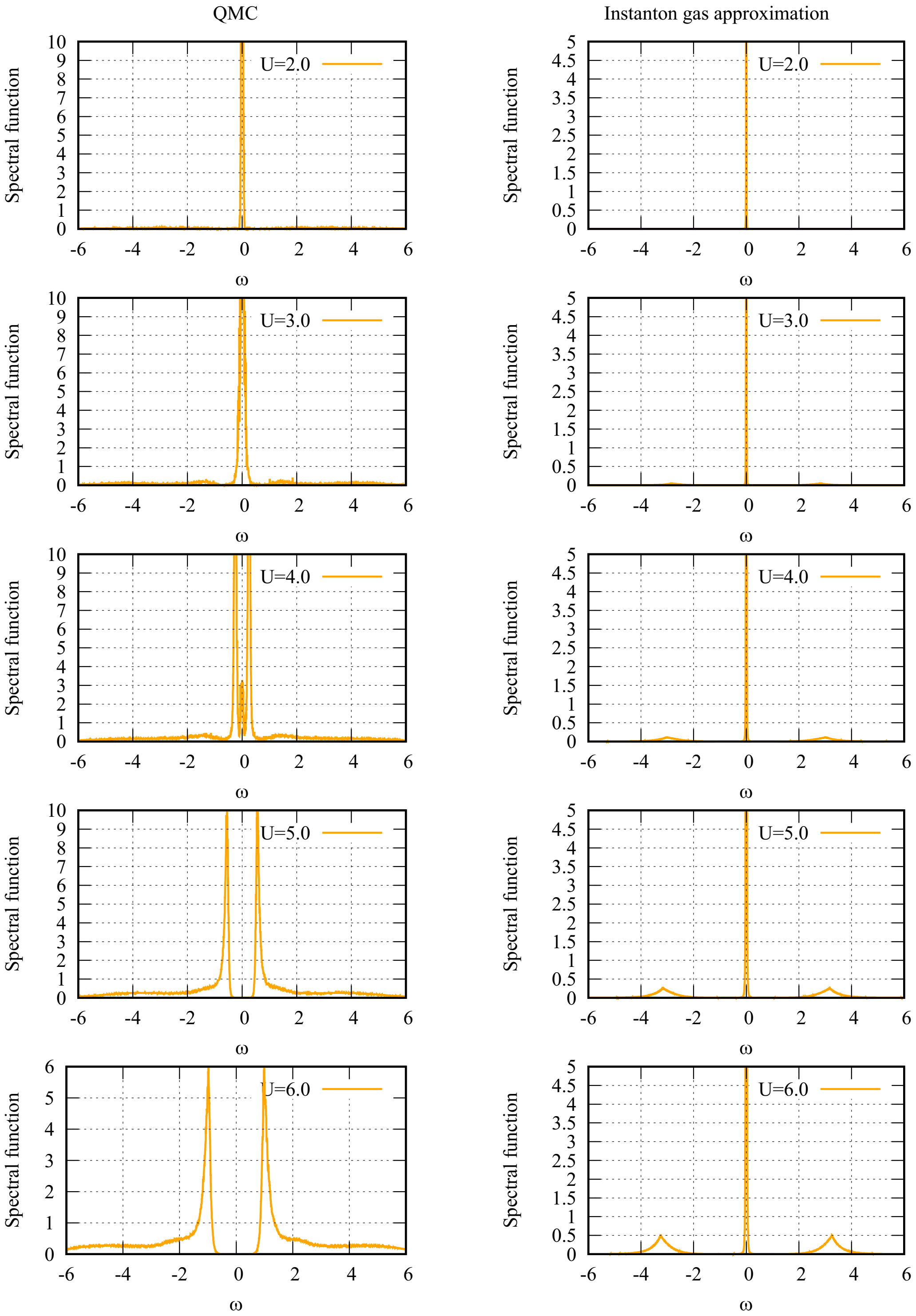

FIG. 15. A comparison of the density of states at the Dirac point obtained from QMC data (left column) with that obtained from the instanton gas model (right column). All calculations correspond to a spatial volume of 12×12 with $\beta\kappa = 20$ and $N_\tau = 256$, while the corresponding interaction strength in units of κ is displayed on each plot. The analytical continuation has been performed with stochastic MEM.

density of the instanton gas for the given range of the interaction strength. Once the configurations have been generated, we average the fermion propagator over these M saddle-point field configurations and obtain the spectral function using the ALF implementation [19] of the stochastic maximum entropy method [49,50].

In accordance with the above discussion, we expect the biggest mismatch between the instanton approach and auxiliary field QMC at low energies; namely, in the vicinity of the Dirac point (see Fig. 15). The QMC results are plotted in the left row, while the results from the instanton gas model data are shown in the right row. As one can see, the QMC results

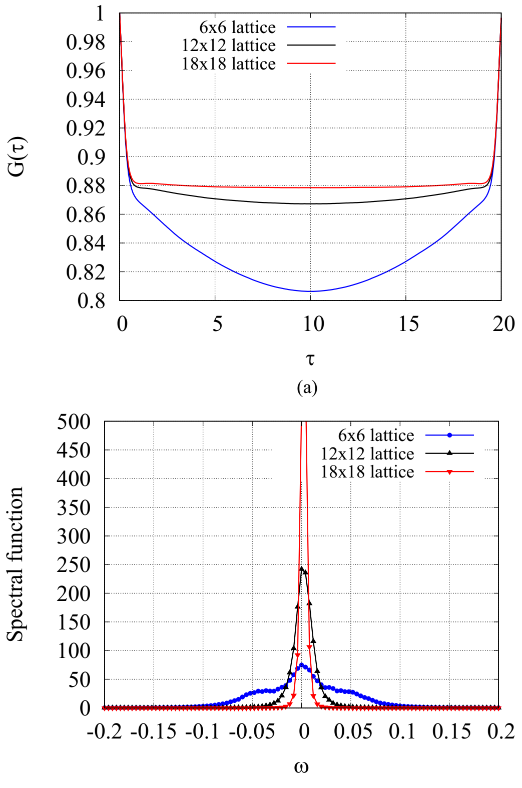

(a)

(b)

FIG. 16. (a) The Euclidean-time fermion propagator at the Dirac point in momentum space, obtained from the instanton gas model with hardcore repulsion. Spatial volumes of 6×6, 12×12, and 18×18 are compared at $U = 6.0\kappa$, with $N_\tau = 256$ in each case. (b) The electron density of states obtained after analytical continuation performed with stochastic MEM.

show the appearance of a mass gap starting from $U \approx 4.0\kappa$, while the spectral function obtained within the instanton gas approximation is always concentrated at zero energy. Thus, the formation of a mass gap cannot be described in this simple saddle-point approximation. This, along with the failure to reproduce long-range AFM order are two features that are not sensitive to the instantons. A more detailed analysis of the spectral functions within the instanton gas approximation is presented in Fig. 16. In this figure, we check the dependence of the spectral functions at the Dirac point on the spatial lattice size. For smaller lattices, we observe noticeable broadening of the spectral function. This broadening is a consequence of the fact that the 6×6 lattice is roughly the size of the cluster of local AFM ordering in the vicinity of the centers of instantons (see Figs. 13 and 1). Once the lattice size increases, the simulations start to reflect the absence of long-range AFM ordering and the width of the spectral function decreases. We thus can conclude that, physically, the increase of the instanton density with increasing U corresponds to the increasing local AFM correlations while still not reproducing the long-range ordering of spins.

As shown in Fig. 2(b), at $U = 6\kappa$, the instanton gas spectral function compares remarkably well with the auxiliary field QMC result of Fig. 2(a), provided that we just shift it by the mass gap. Thus, our instanton approach reproduces the salient features of the high-energy spectral function that can naturally be accounted for within a parton picture of the single-particle spectral function. The upper Hubbard *band* is most pronounced in the vicinity of the Γ point. To quantify this, the relative weight of the upper Hubbard band, we plot the share of the lower peak in the whole spectral function [Fig. 2(c)]. We use the local minimum between peaks as the delimiter. Again, the QMC and instanton gas curves show remarkably similar behavior, and thus we can conclude that the instanton gas model provides an accurate picture of the single-electron spectral functions both in the weak- and strong-coupling limits, away from the Dirac point.

We now provide a detailed study of the spectral function at the Γ point, where high-energy spectral weight is most pronounced. A comparison of the QMC results with those obtained from auxiliary field QMC is shown in Fig. 17. By construction, the instanton approach satisfies the sum rule:

$$\int d\omega A(\boldsymbol{k}, \omega) = \pi. \tag{63}$$

At $U = 0$, all the spectral weight is located at $\omega = \pm 3\kappa$. As one increases the Hubbard U, one observes a clear transfer of spectral weight from this peak to higher frequencies. This phenomena already occurs prior to the magnetic transition and is pronounced both in the QMC and in the instanton gas approach. We have equally checked that the observed transfer of spectral weight at large U is not a finite-size effect. The corresponding data is shown in Fig. 18, where we compared the results for the instanton gas model on spatial lattice volumes of 6×6, 12×12, and 18×18. The observed spectral functions are almost identical, which is a nontrivial check of the instanton gas model. On the whole, the comparison between the QMC and instanton gas approach is very good, especially if a rigid shift is taken into account to accommodate for the mass gap that develops at $U > U_c \simeq 3.8\kappa$. Hence, the instanton gas model does capture the high-energy spectral weight. Within the parton approach, this finds a natural interpretation since the electron corresponds to a composite object that breaks down at high energies, giving rise to incoherent spectral weight.

For a more detailed analysis of the spectral functions at the Γ point, we plot the location of the upper and lower edges—as determined by the peak positions—of the spectral function in Fig. 19. Within an exact solution to the Hubbard model, we expect the charge gap to scale as U in the strong coupling limit, and the width of the spectral function, as defined by the difference in energy between the upper and lower edges of the single electron spectral function, to scale as κ. This statement is supported by numerical exact diagonalization of the *t-J* model in which the charge gap is infinite but the width of support of the single particle spectral function is set by the kinetic energy [43]. As apparent from the data in Fig. 19, we see that the QMC supports this statement since both the lower and upper edges of the spectrum grow as a function of U, but the difference remains, to a first approximation, constant. As argued previously, the instanton approach captures the high-energy physics but fails in the low-energy sector, in the sense that a charge gap is not produced. In fact, for a Dirac system, and excluding exotic physics such as the formation of a quantum spin liquid ground state, a mass gap can only occur

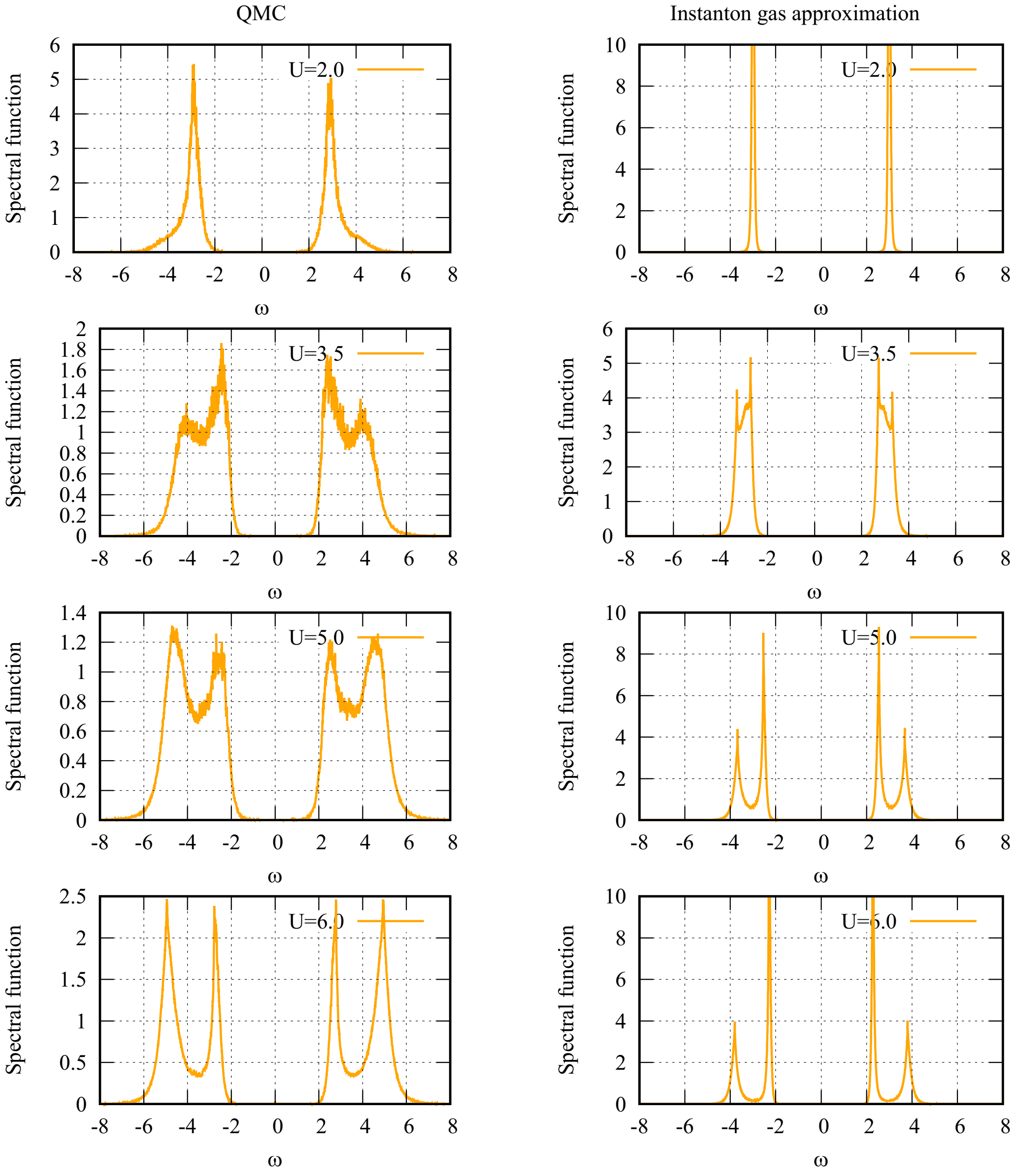

FIG. 17. Spectral functions at the Γ point obtained from QMC data with Ising fields (left column) and from the instanton gas model with hardcore repulsion (right column). The calculations were performed on a 12 × 12 lattice with $\beta\kappa = 20$ and $N_\tau = 256$, while the corresponding interaction strength is shown on each plot.

provided that symmetry breaking occurs. This shortcoming of the instanton approach shows up in Fig. 19: while the upper edge grows as a function of U, the lower edge actually decreases.

VI. SQUARE LATTICE HUBBARD MODEL

We now briefly apply the same techniques to the Hubbard model on the square lattice to investigate the differences and similarities with the hexagonal lattice. The physics of the Hubbard model on the square lattice at the particle-hole symmetric point is different, since a Stoner instability suggests that the AFM insulating phase is present for any infinitesimal U in the ground state [51]. There are, however, some indications [51,52] that there is a crossover from Slater-like to Heisenberg-like fluctuations at around $U = 5\kappa$. Since a partial particle-hole transformation maps the repulsive Hubbard model onto the attractive one, this parallels the BCS to BEC crossover [53].

Now we turn to the picture of the saddle points, obtained with exactly the same procedure as described in Appendix A. At large U, we mainly find the same highly localized instantons, with their density increasing with increasing U. However, the picture is quite different at $U < 5\kappa$: In this case, we observe not only instantons but also *domain-wall* solutions, that are constant in Euclidean time and form barriers that divide the lattice in space. An example of such a solution is shown in Fig. 20(b). It is a spatial map of the charge-coupled auxiliary field $\phi_{x,\tau}$ (we do not show the Euclidean time dynamics, since the field is independent of time). In the

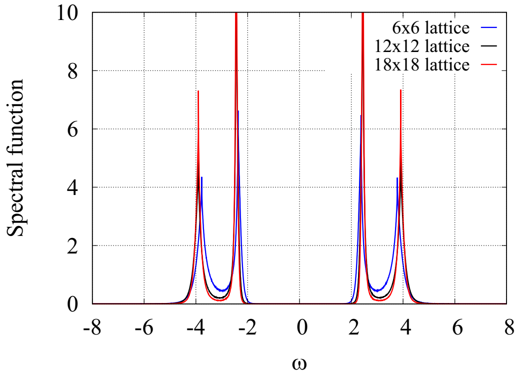

FIG. 18. Comparison of the spectral functions at the Γ point for different spatial volumes in the instanton gas model with hardcore repulsion. The interaction strength is equal to $U = 6.0\kappa$ and inverse temperature $\beta\kappa = 20$.

configuration depicted in this plot, the saddle point consists of two domain walls which intersect at a right angle.

The relative weight of the domain walls, instantons, and the vacuum saddle ($\phi_{x,\tau} = 0$) in the partition function as a function of interaction strength U is shown in Fig. 20(a). At small U, the partition function can be fully described by the integrals attached to the vacuum and *domain-wall* saddles. At larger U, there is a relatively smooth transition to the instanton-dominated region. Interestingly, the crossover between these two regimes coincides with the above-mentioned crossover from a Slater to a Heisenberg antiferromagnet. From the present data, it is remarkable to see that the saddle point approximation captures this crossover. We expect that the connection between the ground state properties and the saddles can be established using the formalism described in Appendix E. However, the detailed study of this subject is beyond the scope of the current paper.

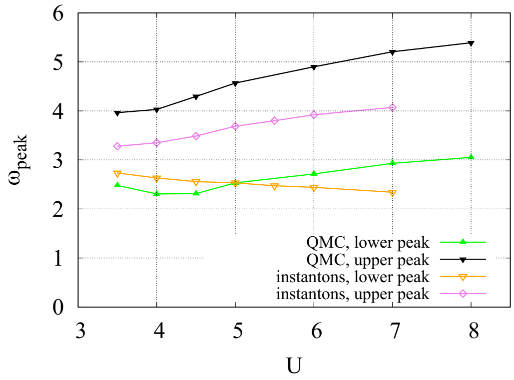

FIG. 19. The energies corresponding to the upper and lower peaks in the single electron spectral function at the Γ point in the strong coupling limit $U > 3.5$, where the two-peak structure becomes apparent (see Fig. 17 for the full profiles). All data were produced on a 12×12 lattice at $N_\tau = 256$ and $\beta\kappa = 20$. The hardcore repulsion model was used for the instanton gas approach.

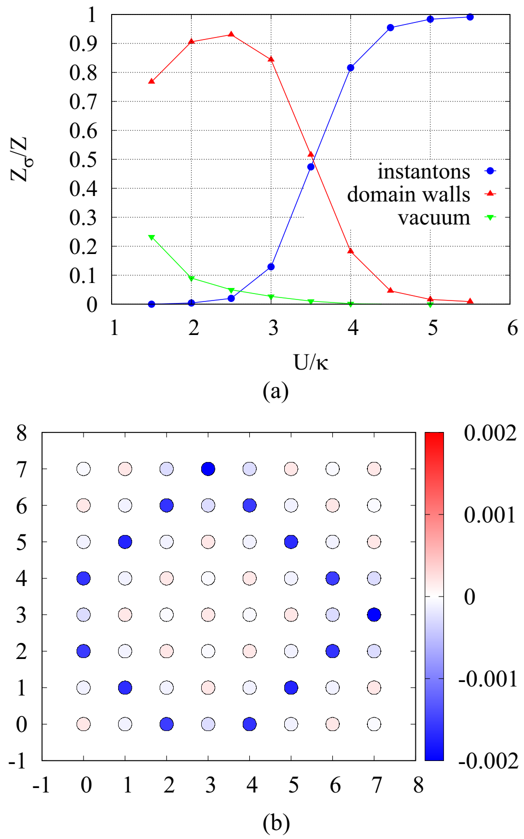

(a)

(b)

FIG. 20. (a) The relative weight of instantons, domain walls, and vacuum saddle in the full partition function for the square lattice Hubbard model. These were obtained from the configurations generated in QMC on the square lattice, followed by the application of GF. The data was generated on a 8×8 square lattice with $\beta\kappa = 20$, $N_\tau = 512$. (b) An example of a domain-wall configuration at $U = 1.5\kappa$. The color scale shows the value of the auxiliary field ϕ.

VII. CONCLUSION

We have considered the exact saddle points for the path integral formulation of the Hubbard model, where the continuous auxiliary field is coupled to the charge density. The saddle points have been obtained both numerically and analytically without restriction to constant fields in space and time. Remarkably, the general saddle-point field configuration can be decomposed into a collection of instantons. An individual instanton is a solution of the classical Euclidean equations of motion for the auxiliary scalar field, which is localized both in space and Euclidean time and determined by taking into account the back reaction of the fermionic determinant.

As a result of the above, we can define a Gaussian approximation to the partition function, where the Gaussian integral is taken around the N-instanton saddle point. This integral has a well-defined continuum limit with respect to the Euclidean time discretization. The study of the two-instanton saddle reveals that the characteristics of this saddle (e.g., action, Hessian, etc.) are almost independent of their relative position such that we can treat instantons as weakly interacting classical pointlike objects in 3D space-time.

Using this knowledge, we have constructed an instanton gas model that can be solved using both analytical approaches and classical GCMC simulations. A comparison with unbiased QMC simulations shows that this model gives correct predictions for the structure of the dominant saddle point. While this feature is probably not so useful at half filling, it would be interesting to extend this approach away from half filling. As was shown in Ref. [12], the instantons for the Hubbard model retain their structure even at nonzero chemical potential. The only difference is that, according to the general logic of the Lefschetz decomposition, these instantons are now shifted in complex space, which means that the auxiliary fields acquire complex values. However, the profiles for both the real and imaginary parts of the auxiliary fields remain localized in space and time. Thus, it would be interesting to construct a similar instanton gas model for these complex field profiles. If successful, we might obtain an accurate prediction for the dominant saddle point even away from half filling. Combined with the demonstrated sharpness of the distribution of the instanton density in the thermodynamic limit, this gives us an opportunity to replace the sum over Lefschetz thimbles by one integral over the thimble attached to the *a priori* known dominant saddle point.

The structure of the saddle points provides a very interesting approximation to the Hubbard model. Given the partition function of the instanton gas, we can use classical Monte Carlo methods to sample it. The instanton configurations can then be translated into auxiliary field configurations for which the fermion determinant and various equal-time and time-displaced correlation functions can be computed. Using this scheme, we can elucidate the physical content of a single instanton located at a space-time point (X, T) by computing the spin-spin and charge-charge correlation functions. The individual instanton generates a local moment and concomitant short-ranged AFM fluctuations in space. The instanton approximation fails to capture long-ranged AFM order but certainly describes metallic states in the presence of short-ranged magnetic fluctuations. By computing the single-particle spectral function, we have observed remarkable agreement with unbiased quantum Monte Carlo results provided that, in the magnetically ordered state, we account for the mass gap by a rigid shift in frequency.

As mentioned above, the saddle-point approximation fails to capture the formation of long-range AFM order. However, this failure might not be so important away from half filling, since the long-range order rapidly breaks down with increased doping. Thus, the proposed instanton gas approach, despite its deficiencies at half filling, might be even more suitable for the approximate calculations at finite chemical potential, where a severe sign problem hinders our ability to get unbiased results using QMC simulations.

The instanton gas approach is a thermodynamically well-defined approximation such that low-temperature properties of metals subject to AFM fluctuations can be investigated. In this context, it is very desirable and feasible to consider the Hubbard model on the square lattice at half-filling and in the strong-coupling limit, where we observe the instanton structure of the path integral. The lack of long-range magnetic order actually plays to our advantage since a *trivial* gap will not open even at the particle-hole symmetric point where the negative sign problem is absent. The properties of this metallic state and its relation to theories of nearly AFM Fermi liquids reviewed in Ref. [54] certainly deserves further attention.

ACKNOWLEDGMENTS

Computational resources were provided by the Gauss Centre for Supercomputing e.V. [55] through the John von Neumann Institute for Computing (NIC) on the GCS Supercomputer JUWELS [56] at Jülich Supercomputing Centre (JSC). This work also benefited from access to the Irène Joliot-Curie supercomputer of the Très Grand Center de Calcul (TGCC) of the Commissariat à l'Énergie Atomique et aux Énergies Alternatives (CEA) in France as part of the Project No. gen2271 awarded by GENCI (Grand Equipement National de Calcul Intensif). M.U. thanks the DFG for financial support under Project No. UL444/2-1. F.F.A. acknowledges financial support from the DFG through the Würzburg-Dresden Cluster of Excellence on Complexity and Topology in Quantum Matter–ct.qmat (EXC 2147, Project ID No. 39085490) and No. SFB1170 on Topological and Correlated Electronics at Surfaces and Interfaces. C.W. acknowledges support by the Deutsche Forschungsgemeinschaft (DFG, German Research Foundation) through No CRC-TR 211, Strong-Interaction Matter under Extreme Conditions, Project No. 315477589–TRR 211.

APPENDIX A: OBSERVATION OF INSTANTONS IN THE QMC DATA

This Appendix describes technical aspects regarding the determination of saddle points from the QMC data. Since we can only use continuous auxiliary fields to construct the saddle-point approximation, we employ the standard technique of updating the continuous fields in QMC simulations—the HMC. This updating procedure is based on Hamiltonian dynamics for the auxiliary field. The main issue is the absence of ergodicity in such simulations for the Hubbard model when only one auxiliary field is used [57]. Following Ref. [57], we employ the two-field approach to overcome this issue. In this approach, the interaction term is split into two terms using the Fierz identities

$$\frac{U}{2}\hat{q}_{\boldsymbol{x}}^2 = \frac{\alpha U}{2}\hat{q}_{\boldsymbol{x}}^2 - \frac{(1-\alpha)U}{2}\hat{s}_{\boldsymbol{x}}^2 + (1-\alpha)U\hat{s}_{\boldsymbol{x}}, \tag{A1}$$

where $\hat{s}_x = \hat{n}_{\boldsymbol{x},\mathrm{el}} + \hat{n}_{\boldsymbol{x},\mathrm{h}}$ is the spin operator and $\alpha \in [0, 1]$ is an extra, nonphysical parameter. Thus, in addition to Eq. (5), for $\alpha \neq 1$, one must also introduce a second auxiliary field coupled to the spin

$$e^{\frac{\Delta\tau U(1-\alpha)}{2}\hat{s}_{\boldsymbol{x}}^2} \cong \int d\chi_{\boldsymbol{x}}\, e^{-\frac{\chi_{\boldsymbol{x}}^2}{2\Delta\tau U(1-\alpha)}} e^{\chi_{\boldsymbol{x}}\hat{s}_{\boldsymbol{x}}}. \tag{A2}$$

This generalized HS transformation serves several purposes. It solves the ergodicity problems associated with the HMC as infinite energy barriers appear which separate regions where the electron(hole) determinant has different signs. This was first noted in Refs. [58] and further applied in Refs. [57,59]. This particular representation is also advantageous as it works for nonlocal interactions, unlike methods that employ discrete auxiliary fields. The form of the functional integral is slightly

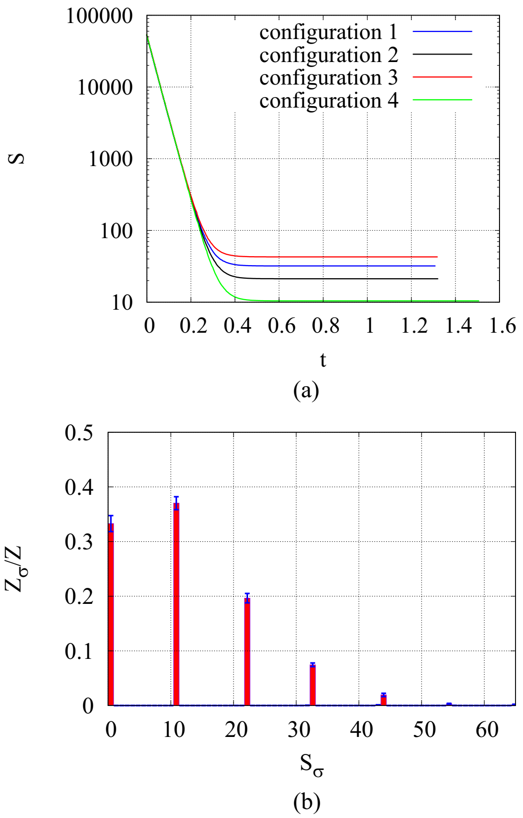

FIG. 21. (a) The profile of the action during the *downward* flow to the saddle points. This procedure essentially amounts to the solution of the gradient flow equation in Eq. (13). Four different configurations are shown, each ending at a different saddle. (b) The distribution for the final actions obtained after the application of the downward gradient flow to the set of configurations generated with HMC. These calculations were performed on a 12 × 12 lattice with $\beta\kappa = 20$ and $N_\tau = 512$, with interaction strength $U = 2.0\kappa$ and $\alpha = 0.99$.

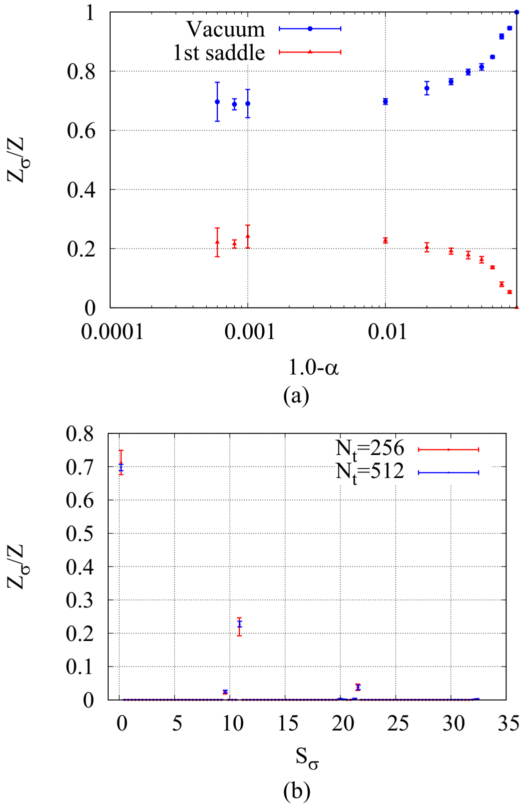

FIG. 22. (a) Relative weight of the thimble attached to the first nontrivial saddle with respect to the full partition function, Z_1/Z, as a function of the α parameter. These calculations were performed on a 6 × 6 lattice with $N_\tau = 512$, $\beta\kappa = 20$. (b) A comparison of the histograms obtained for $N_\tau = 256$ and $N_\tau = 512$ with other parameters fixed (6 × 6 lattice, $\beta\kappa = 20$, $\alpha = 0.99$). The interaction strength is fixed at $U = 2.0\kappa$ for all plots.

modified when the spin-coupled field is introduced following Refs. [57,60,61], taking the form

$$\mathcal{Z} = \int \mathcal{D}\phi_{x,\tau}\, \mathcal{D}\chi_{x,\tau}\, e^{-S_\alpha} \det M_{\mathrm{el}} \det M_{\mathrm{h}},$$

$$S_\alpha[\phi_{x,\tau}, \chi_{x,\tau}] = \sum_{x,\tau}\left[\frac{\phi^2_{x,\tau}}{2\alpha\Delta\tau U} + \frac{(\chi_{x,\tau} - (1-\alpha)\Delta\tau U)^2}{2(1-\alpha)\Delta\tau U}\right], \tag{A3}$$

where the determinants of the fermionic operators are given by

$$\det M_{\mathrm{el,h}} = \det\left[I + \prod_{\tau=1}^{N_\tau} e^{-\Delta\tau h}\tilde{D}_\tau\right]. \tag{A4}$$

Here we have introduced the matrices $\tilde{D}_\tau \equiv \mathrm{diag}\,(e^{\pm i\phi_{x,\tau} + \chi_{x,\tau}})$, in analogy with the case which only involved the charge-coupled field.

The two-field formalism solves the ergodicity issues in the HMC simulations. Therefore, we are free to use the action in Eq. (6) in HMC both for the generation of configurations and for the subsequent solution of the GF equations. Several examples depicting the flow-time history of the action during GF are shown in the Fig. 21(a). However, we are interested in the case of $\alpha = 1$, whereby only the charge-coupled field ϕ is present. In practice, we recover this limit by setting $\alpha \approx 1$ and taking the limit $\alpha \to 1$. If α is reasonably close to 1, we already recover the equidistant discrete peaks in the final histogram for the action after GF (see Fig. 21(b) and more detailed study [12]). The weights of the peaks are stable in the limit $\alpha \to 1$, as demonstrated in Fig. 22(a). Thus, our strategy can indeed be used to determine the structure of saddle points in the limit $\alpha = 1$. We always use $\alpha = 0.99$ in the QMC calculations presented in this paper.

As a final check, we repeat the simulations for the same physical parameters but at different values of N_τ. This is to ensure that systematic effects due to discretization in Euclidean time are under control. As one can see in Fig. 22(b), the histograms do not change. We can therefore conclude that the continuum limit $\Delta\tau \to 0$ indeed exists and with our typical setup of $\beta\kappa = 20$ and $N_\tau = 256$, we are reasonably close to it.

APPENDIX B: ANALYTICAL SOLUTION FOR INDIVIDUAL INSTANTON

In developing the functional integral approach to the Hubbard model, we have integrated out the fermionic degrees of freedom leaving us with a theory that only involves bosonic degrees of freedom. The tradeoff is that the theory involves a nonlocal quantity, namely, the fermionic determinant. To obtain the saddle-point equations for the auxiliary field, ϕ, we must first re-exponentiate the fermion determinant which gives the following form for the effective Euclidean action:

$$S = S_B - \ln(\det M_{\mathrm{el}} \det M_{\mathrm{h}}). \tag{B1}$$

To make the process of taking the continuum limit in Euclidean time clearer, we make the trivial rescaling $\phi_{\boldsymbol{x},\tau} \to \Delta\tau\phi_{\boldsymbol{x},\tau}$. As a result, the bosonic action reads

$$S_B[\phi] = \sum_{\boldsymbol{x},\tau} \frac{\phi^2_{\boldsymbol{x},\tau}\Delta\tau}{2U}, \tag{B2}$$

and the exponents in the even blocks of the fermionic determinants are written as $D_{2\tau} \equiv \mathrm{diag}\,(e^{i\Delta\tau\phi_{\boldsymbol{x},\tau}})$.

From Eq. (B2), one sees that the bosonic part of the action, S_B, is Gaussian, and thus any potentially nontrivial solution to the saddle-point equations for the auxiliary fields can only be achieved by taking into account the contribution from the fermion determinant in the background of a given bosonic field configuration.

To obtain the saddle-point equation for the bosonic field $\phi_{\boldsymbol{x},\tau}$, it is convenient to express the electron (hole) operator in the following basis:

$$M_{\mathrm{el}} = \begin{pmatrix} I & D_1 & 0 & 0 & \dots & \dots & 0 \\ 0 & I & D_2 & 0 & \dots & \dots & 0 \\ \dots & \dots & \ddots & \ddots & \dots & \dots & \dots \\ \dots & \dots & \dots & I & D_{2\tau} & \dots & \dots \\ \dots & \dots & \dots & \dots & I & D_{2\tau+1} & \dots \\ \dots & \dots & \dots & \dots & \dots & \ddots & \ddots \\ -D_{2N_\tau} & \dots & \dots & \dots & \dots & \dots & I \end{pmatrix}, \tag{B3}$$

where each entry represents a block of size $N_S \times N_S$. In a similar way, the fermion propagator can be written in terms of $N_S \times N_S$ blocks:

$$M_{\mathrm{el}}^{-1} = \begin{pmatrix} g^1 & \dots & \dots & \dots & \dots & \dots & \bar{g}^{2N_\tau} \\ \bar{g}^1 & g^2 & \dots & \dots & \dots & \dots & \dots \\ \dots & \bar{g}^2 & g^3 & \dots & \dots & \dots & \dots \\ \dots & \dots & \ddots & \ddots & \dots & \dots & \dots \\ \dots & \dots & \dots & \bar{g}^\tau & g^\tau & \dots & \dots \\ \dots & \dots & \dots & \dots & \ddots & \ddots & \dots \\ \dots & \dots & \dots & \dots & \dots & \dots & g^{2N_\tau} \end{pmatrix}. \tag{B4}$$

The off-diagonal blocks $\bar{g}_i$ satisfy the following relation:

$$\bar{g}^{\tau+1} = D^{-1}_{\tau+1}\bar{g}^\tau D_\tau, \tag{B5}$$

which is reminiscent of the *forward* propagation relation for the equal-time Green's function in the BSS-QMC algorithm [62]. One can relate the blocks in Eq. (B4) on the diagonal to the blocks below the diagonal using

$$g^\tau = I - D_\tau \bar{g}^\tau, \tag{B6}$$

which simply follows from $M_{\mathrm{el}}M_{\mathrm{el}}^{-1} = I$. We note that the Euclidean time index for the blocks g^τ and $\bar{g}^\tau$ takes values from 1 to $2N_\tau$, in accordance with the employed scheme for the decomposition of the Boltzmann weight at each time slice. Using the well-known relation for the derivative of the logarithm of the fermion determinant

$$\frac{\partial \ln \det M}{\partial \phi_{\boldsymbol{x},\tau}} = \mathrm{Tr}\left(M^{-1}\frac{\partial M}{\partial \phi_{\boldsymbol{x},\tau}}\right), \tag{B7}$$

one can obtain the following expression for the derivative of the action Eq. (B1) with respect to the bosonic auxiliary fields:

$$\begin{aligned} \frac{\partial S}{\partial \phi_{\boldsymbol{x},\tau}} &= \Delta\tau\frac{\phi_{\boldsymbol{x},\tau}}{U} \\ &\quad - \Delta\tau\left(\bar{g}^{2\tau}_{\boldsymbol{xx}} i e^{i\Delta\tau\phi_{\boldsymbol{x},\tau}} - \left(\bar{g}^{2\tau}_{\boldsymbol{xx}}\right)^* i e^{-i\Delta\tau\phi_{\boldsymbol{x},\tau}}\right). \end{aligned} \tag{B8}$$

This relation is used not only in numerically determining the fermionic *force* in HMC calculations but can also be used to determine the saddle points of Eq. (B1). These are obtained from the relation

$$\frac{\partial S}{\partial \phi_{\boldsymbol{x},\tau}} = 0. \tag{B9}$$

One then obtains the following form for the saddle-point equation:

$$\phi_{\boldsymbol{x},\tau} = -U\,\mathrm{Im}\left\{\bar{g}^{2\tau}_{xx} e^{i\Delta\tau\phi_{\boldsymbol{x},\tau}}\right\}, \tag{B10}$$

which relates the bosonic field to the Green's function. In the continuum limit, $\Delta\tau \to 0$, the saddle point Eq. (B10) becomes

$$\phi_{\boldsymbol{x},\tau} = -U\,\mathrm{Im}\,\bar{g}^{2\tau}_{\boldsymbol{xx}}, \tag{B11}$$

where we have taken into account that $\mathrm{Re}\,\bar{g}^\tau_{xx} = \frac{1}{2}$, for all τ, which follows from particle-hole symmetry. To close the system of equations, we add the equations for the fermionic propagator at a given background of the auxiliary field. Applying the BSS-QMC forward propagation relation in Eq. (B5) twice, one obtains the following equations:

$$\begin{aligned} \bar{g}^{2\tau+2} &= D^{-1}_{2\tau+2}D^{-1}_{2\tau+1}\bar{g}^{2\tau}D_{2\tau}D_{2\tau+1}, \\ &= \mathrm{diag}\,(e^{-i\Delta\tau\phi_{\boldsymbol{x},\tau+1}})e^{\Delta\tau h}\bar{g}^{2\tau}\,\mathrm{diag}\,(e^{i\Delta\tau\phi_{\boldsymbol{x},\tau}})e^{-\Delta\tau h}. \end{aligned} \tag{B12}$$

The various terms on the right-hand side of Eq. (B12) can be expanded to linear order in $\Delta\tau$. Then, remembering the saddle-point relation Eq. (B11), ϕ can be eliminated in favor of $\bar{g}$. Finally, after taking the continuum limit, $\Delta\tau \to 0$, one obtains

$$\begin{aligned} \frac{dg_{\boldsymbol{xx}}(\tau)}{d\tau} &= -\kappa\sum_{\langle \boldsymbol{x},\boldsymbol{y}\rangle}(g_{\boldsymbol{xy}}(\tau) - g_{\boldsymbol{yx}}(\tau)) \\ \frac{dg_{\boldsymbol{xy}}(\tau)}{d\tau} &= iU g_{\boldsymbol{xy}}(\mathrm{Im}\,g_{\boldsymbol{xx}}(\tau) - \mathrm{Im}\,g_{\boldsymbol{yy}}(\tau)) \\ &\quad - \kappa\left(\sum_{\langle \boldsymbol{z},\boldsymbol{x}\rangle} g_{\boldsymbol{xz}}(\tau) - \sum_{\langle \boldsymbol{z},\boldsymbol{y}\rangle} g_{\boldsymbol{zy}}(\tau)\right). \end{aligned} \tag{B13}$$

This set of equations completely determines the semiclassical description of fermions propagating in the background of an instanton. In particular, the correlations between winding and the number of instantons and anti-instantons can be understood from this set of equations (see below).

Alternatively, this set of equations can also be derived from the Euclidean-time Heisenberg equations of motion

$$\frac{d\hat{A}}{d\tau} = [\hat{H}, \hat{A}], \tag{B14}$$

where we consider the following fermion bilinear operators:

$$\hat{A} = \hat{a}^\dagger_x \hat{a}_y,\ \hat{b}^\dagger_x \hat{b}_y,\ \hat{a}^\dagger_x \hat{a}_x,\ \hat{b}^\dagger_x \hat{b}_x \tag{B15}$$

and the Hamiltonian $\hat{H}$ is taken from Eq. (1).

After substitution of Eq. (B15) into (B14), the operator analog of Eq. (B13) can be written as

$$\begin{aligned}\frac{d\hat{a}^\dagger_x \hat{a}_x}{d\tau} &= -\kappa \sum_{\langle x,y\rangle} (\hat{a}^\dagger_y \hat{a}_x - \hat{a}^\dagger_x \hat{a}_y)\\ \frac{d\hat{a}^\dagger_x \hat{a}_y}{d\tau} &= U \hat{a}^\dagger_y \hat{a}_x (\hat{b}^\dagger_x \hat{b}_x - \hat{b}^\dagger_y \hat{b}_y)\\ &\quad - \kappa \left(\sum_{\langle z,y\rangle} \hat{a}^\dagger_z \hat{a}_x - \sum_{\langle z,x\rangle} \hat{a}^\dagger_y \hat{a}_z \right)\end{aligned} \tag{B16}$$

These operator relations, when applied to expectation values, take the exact same form as Eq. (B13) in the mean-field limit. As usual, when working in the mean-field approximation, one assumes that the expectation of four-fermion terms factorize

$$\langle \hat{a}^\dagger_x \hat{a}_y \hat{b}^\dagger_x \hat{b}_x \rangle \approx \langle \hat{a}^\dagger_x \hat{a}_y \rangle \langle \hat{b}^\dagger_x \hat{b}_x \rangle. \tag{B17}$$

After this factorization, we arrive at exactly the same equations as Eq. (B13), taking into account that $g_{xy} = \langle \hat{a}_x \hat{a}^\dagger_y \rangle$.

The system of equations Eq. (B13) can be further simplified if we take into account the fact that the exact instanton solutions observed in the QMC results of the previous section are ultralocal in space, namely, the bosonic field $\phi_{x,\tau}$ is sharply concentrated (measured by its magnitude $|\phi|$) at one lattice site. A further simplification occurs if one takes into account the C_3 symmetry of the hexagonal lattice, and the rapid decay of the equal-time fermionic propagator with increased spatial separation between source and sink. It turns out that this rapid decay is also a consequence of the observed locality of the instanton field configurations. In fact, the propagator is identical to that of freely propagating fermions everywhere except in the close vicinity of the instanton *core*. Our assumptions about the equal-time fermion Green's function, computed in the background of an instanton centered at spatial lattice site x, can be summarized as follows: we take into account only $\operatorname{Im} g_{xx}(\tau)$ and $g_{\langle xy\rangle}(\tau)$, and the latter components of the Green's function are equal for all three nearest neighbors.

Under these assumptions, Eq. (B13) simplifies greatly and takes the form

$$\begin{aligned}&\frac{d}{d\tau} \operatorname{Im} g_{xx}(\tau) = 6\kappa \operatorname{Im} g_{xy}(\tau)\\ &\frac{d}{d\tau} \operatorname{Im} g_{xy}(\tau) = iU g_{xy}(\tau) \operatorname{Im} g_{xx}(\tau) + i\kappa \operatorname{Im} g_{xx}(\tau).\end{aligned} \tag{B18}$$

Separating the real and imaginary parts of the above equations gives the following set of coupled, first-order differential equations:

$$\dot{d}(\tau) = 6\kappa b(\tau), \tag{B19}$$

$$\dot{b}(\tau) = U d(\tau)(a(\tau) + G^{-1}), \tag{B20}$$

$$\dot{a}(\tau) = -U \dot{b}(\tau) d(\tau), \tag{B21}$$

where $g_{xy}(\tau) = a(\tau) + ib(\tau)$, $\operatorname{Im} g_{xx} = d(\tau)$, and we have defined the dimensionless ratio $G \equiv U/\kappa$. From Eqs. (B20) and (B21), it is straightforward to see that the solutions can be written in the form

$$a(\tau) = -G^{-1} + R\cos\theta(\tau), \tag{B22}$$

$$b(\tau) = R\sin\theta(\tau), \tag{B23}$$

$$d(\tau) = \frac{\dot{\theta}(\tau)}{U}, \tag{B24}$$

where R is a dimensionless constant determined by the initial conditions far away from the center of instanton, where the Green's function $g_{xy}(\tau)$ tends to its vacuum value. For the imaginary part, this means that $\operatorname{Im} g_{xy} = b \to 0$, thus $\theta \to 0$. For the real part, this means that $\operatorname{Re} g_{xy}|_{\text{vac}} = -G^{-1} + R$. Finally, inserting Eq. (B24) into Eq. (B19), one obtains a second-order differential equation for the angle

$$\ddot{\theta}(s) = \sin\theta(s), \tag{B25}$$

where we have introduced the rescaled Euclidean time $s \equiv \tau\sqrt{6\kappa U R}$. One recognizes Eq. (B25) as the equation of motion satisfied by a physical pendulum where the angle between the vertical and the pendulum has been shifted by π. Thus, the vacuum corresponds to the upper position of the pendulum, and the instanton solution corresponds to the trajectory $\theta(\tau)$, which starts near the upper position of the pendulum, spends a large time in its vicinity, then quickly performs a rotation through the bottom position. If the initial velocity $\dot{\theta}$ is large enough to make one or more full rotations during the period $s_{\text{full}} = \beta\sqrt{6\kappa U R}$, we have a solution with N_{inst} instantons. If the initial velocity is not large enough to pass over the highest point, the pendulum goes in the opposite direction during the second half of the period and we have an instanton-anti-instanton solution.

The number of instantons can be connected to the initial conditions of the pendulum using the analogy with classical mechanics. Energy conservation in this case takes the form

$$\frac{\dot{\theta}^2}{2} + \cos\theta = E_0. \tag{B26}$$

Then, the initial conditions for the N_{inst} solution can be written as $\theta|_{\tau=0} = 0$, $\dot{\theta}|_{\tau=0} = \sqrt{2(E_0 - 1)}$, and E_0 is defined by the number of instantons:

$$\frac{s_{\text{full}}}{N_{\text{inst}}} = 2\int_0^\pi \frac{d\theta}{\sqrt{2(E_0 - \cos\theta)}}. \tag{B27}$$

Example solutions of Eq. (B25), with initial conditions corresponding to a single instanton and instanton-anti-instanton pair are shown in Fig. 23. One can see how the single instanton solution corresponds to the transition of θ angle between two

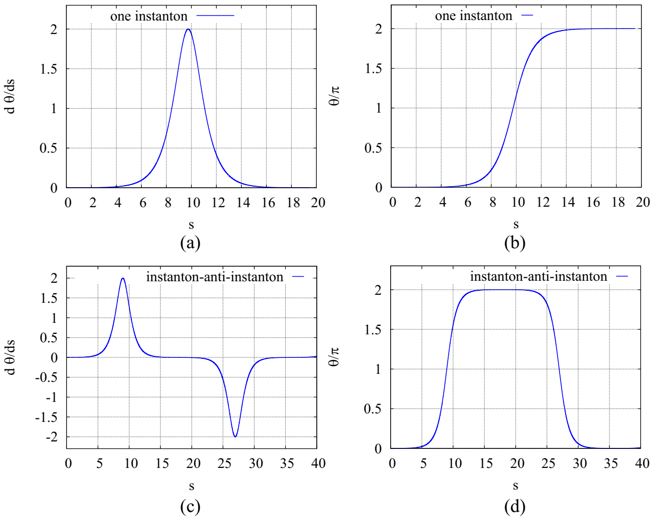

(a) (b)

(c) (d)

FIG. 23. Analytical profiles for instantons obtained from Eq. (B25) for the case of single-instanton [(a), (b)] and instanton-anti-instanton [(c), (d)] solutions. (a) and (c) show the derivative $\dot{\theta}$, while the plots (b) and (d) show the θ angle itself.

equivalent values 0 and 2π, while θ returns to 0 in the case of the instanton-anti-instanton saddle. This observation allows us to introduce the winding number

$$W = \frac{1}{2\pi}\int_0^\beta d\tau\theta(\tau), \tag{B28}$$

which is equal to the difference between the number of instantons and anti-instantons at a given site.

APPENDIX C: HESSIANS FOR *N*-INSTANTON SADDLE POINTS

In this Appendix, the properties of the Hessians around saddle points containing one or more instantons are discussed in further detail. This is necessary, as the treatment of the Hessian is a crucial ingredient of the instanton gas model.

For the construction of the analytical saddle point approximation, we need the ratio of the determinants for the one-instanton saddle and the vacuum saddle. This follows from the fact that all the weights of the nontrivial saddles can be computed in relation to the weight of the trivial vacuum saddle point. Thus, after excluding the zero mode corresponding to the translations in Euclidean time direction Eq. (27), we arrive at the expression

$$\frac{\det \mathcal{H}^{(1)}_{\perp}}{\det \mathcal{H}^{(0)}} = \det(\tilde{\mathcal{H}}^{(1)}_{\perp}) \ = \det((\mathcal{H}^{(1)} + \mathcal{P}^{(1)})(\mathcal{H}^{(0)})^{-1}). \tag{C1}$$

With high accuracy, the projection operator $\mathcal{P}^{(1)}$ to the zero mode direction can be computed through a finite-difference derivative of the instanton field configuration in the Euclidean time direction. This is due to the fact that this derivative approximates the direction which is tangent to the valley in configuration space, which is formed by the degenerate saddle

$$\mathcal{P}^{(1)}_{ij} = \frac{\mathcal{V}_i\mathcal{V}_j}{|\mathcal{V}|^2}, \tag{C2}$$

$$\mathcal{V}_{i(\boldsymbol{x},\tau)} = \phi^{(X,T)}_{\boldsymbol{x},\tau} - \phi^{(X,T+\Delta\tau)}_{\boldsymbol{x},\tau}. \tag{C3}$$

Here (X, T) refers to the location of the instanton center, and the one-dimensional indices are related to the $2+1$D coordinate $(\boldsymbol{x}, \tau)$ via the expression

$$i = 2N_1N_2\tau + x_0N_1N_2 + x_1N_2 + x_2, \tag{C4}$$

with

$$x_1 = 0...N_1 - 1, \quad x_2 = 0...N_2 - 1, \quad x_0 = 0, 1, \tag{C5}$$

being the two 2D coordinates and sublattice indices defining the spatial position of the lattice site. Here N_1 and N_2 are the lattice sizes in the two spatial directions.

Due to the fact that the instanton configurations are local, the reduced Hessian $\tilde{\mathcal{H}}^{(1)}_{\perp}$ matrix is quite sparse: If the second derivative involves the fields far away of the center of the instanton, the corresponding elements of $\mathcal{H}^{(1)}$ are indistinguishable from the ones in $\mathcal{H}^{(1)}$ and they compensate each other in Eq. (C1).

To demonstrate the sparsity of the $\tilde{\mathcal{H}}^{(1)}_{\perp}$ matrix, we display a visualization of its elements $(\tilde{\mathcal{H}}^{(1)}_{\perp})_{ij}$ in Fig. 24(a). The indices i, j are connected to the corresponding $2+1$D coordinates of the fields via the same expressions Eq. (C4). Figure 24(a) shows that the matrix is indeed quite sparse: Elements, which substantially deviate from zero are located along the main diagonal and in the vicinity of the index which maps back to the coordinates of the center of the instanton. In fact, we have checked that it is sufficient to compute the determinant of the small block encompassing the center of the instanton, illustrated by the red rectangle in Fig. 24(a).

Now let us now consider the two-instanton saddle point. Unlike the previous consideration in Sec. III B, we neglect the interaction effects. This means that we assume that the instantons are far away from each other (which is generally true for the saddles with a low density of instantons), and we neglect the change in the action caused by the shift of one instanton with respect to another. Thus, there are two zero modes and the reduced Hessian $\tilde{\mathcal{H}}^{(2)}_{\perp}$ for the two-instanton saddle point is defined as

$$\frac{\det \mathcal{H}^{(2)}_{\perp}}{\det \mathcal{H}^{(0)}} = \det(\tilde{\mathcal{H}}^{(2)}_{\perp}) \ = \det((\mathcal{H}^{(2)} + \mathcal{P}^{(1)} + \mathcal{P}^{(2)})(\mathcal{H}^{(0)})^{-1}), \tag{C6}$$

where the projectors to the zero modes are computed via finite differences corresponding to the shifts of only one of the two instantons:

$$\begin{aligned}\mathcal{P}^{(I)}_{ij} &= \frac{\mathcal{V}^{(I)}_i\mathcal{V}^{(I)}_j}{|\mathcal{V}^{(I)}|^2}\mathcal{V}^{(1)}_{i(\boldsymbol{x},\tau)} \\ &= \phi^{((X^{(1)},T^{(1)}),(X^{(2)},T^{(2)}))}_{\boldsymbol{x},\tau} - \phi^{((X^{(1)},T^{(1)}+\Delta\tau),(X^{(2)},T^{(2)}))}_{\boldsymbol{x},\tau}\mathcal{V}^{(2)}_{i(\boldsymbol{x},\tau)} \\ &= \phi^{((X^{(1)},T^{(1)}),(X^{(2)},T^{(2)}))}_{\boldsymbol{x},\tau} - \phi^{((X^{(1)},T^{(1)}),(X^{(2)},T^{(2)}+\Delta\tau))}_{\boldsymbol{x},\tau}.\end{aligned} \tag{C7}$$

Here $\phi^{((X^{(1)},T^{(1)}),(X^{(2)},T^{(2)}))}_{\boldsymbol{x},\tau}$ refers to the field configuration for two instantons, whose centers are located at the points $(X^{(1)}, T^{(1)})$ and $(X^{(2)}, T^{(2)})$.

The reduced Hessian matrix, $\tilde{\mathcal{H}}^{(2)}_{\perp}$, is shown in Fig. 24(b). If the instantons are far away from each other, the identical nonzero blocks corresponding to the single-instanton configurations are split along the main diagonal. This means that

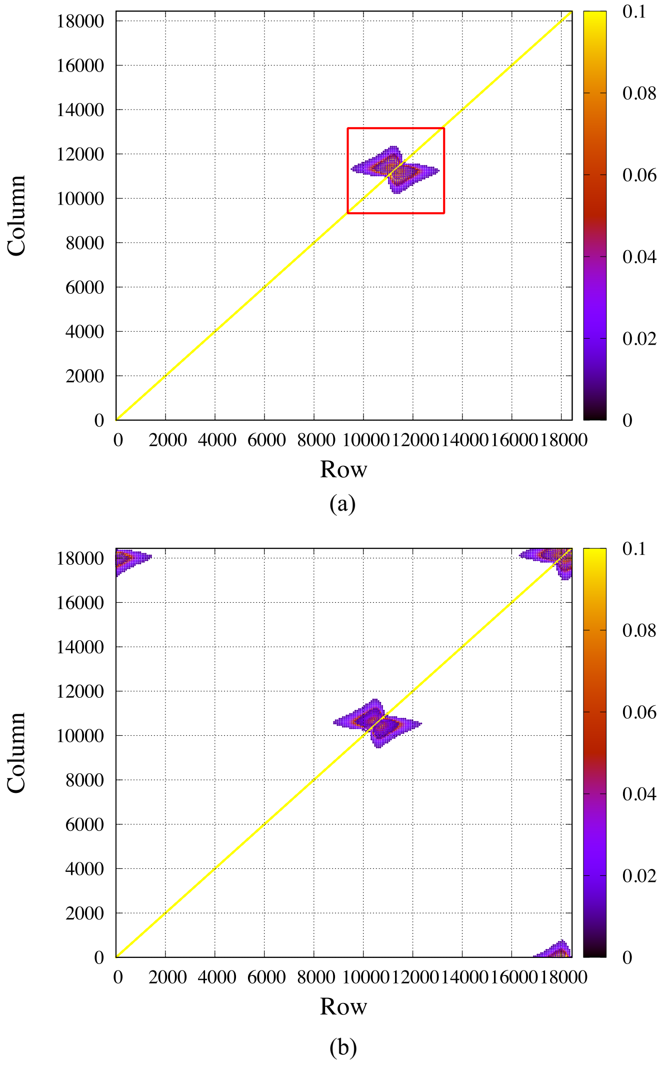

(a)

(b)

FIG. 24. (a) Absolute values of the elements of the reduced Hessian for the one-instanton saddle. The red rectangle denotes the region of the Hessian matrix which is sufficient to calculate the full determinant with high precision. (b) The elements of the reduced Hessian for the two-instanton saddle. To highlight the most important part of the matrix, we only plot the points where the element of the matrix is larger than 0.01. The conversion of the 2 + 1D coordinates to a linear index is done according to the rule Eq. (C4). These calculations were performed on a 6×6 lattice with $N_\tau = 256$, $\beta\kappa = 20$, $U = 5.0\kappa$.

within the approximation of noninteracting instantons, the determinant of the reduced Hessian $\tilde{\mathcal{H}}_\perp^{(N)}$ for the N-instanton saddle point can be approximately computed as

$$\frac{\det \mathcal{H}_\perp^{(N)}}{\det \mathcal{H}^{(0)}} \approx [\det((\mathcal{H}^{(1)} + \mathcal{P}^{(1)})(\mathcal{H}^{(0)})^{-1})]^N. \tag{C8}$$

Due to its simplicity, this expression will be used in the construction of the analytical partition function for the instanton gas model. A numerical proof of this expression is presented in Fig. 25.

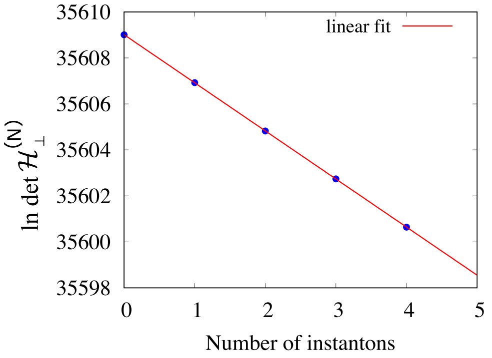

FIG. 25. Numerical proof for the Eq. (C8). $\ln\det\mathcal{H}^{(0)}$ is shown for the vacuum, and $\ln\det\mathcal{H}_\perp^{(N)}$ is shown for the N-instanton saddle. The calculations were performed on a 6×6 lattice with $\beta\kappa = 20$, $U = 2\kappa$ and $N_\tau = 256$.

APPENDIX D: GRAND CANONICAL MONTE CARLO FOR INSTANTON GAS MODEL

In this Appendix, we describe the algorithm used for sampling the instanton gas model with the grand canonical partition function given by Eq. (51). The state of the system is described by the set of N coordinates $\{X_i, T_i\}$, $i = 1...N$. $T_i \in (0, \beta)$ is the Euclidean time coordinate of the ith instanton and

$$X_i = (\nu_i, \boldsymbol{r}_i), \tag{D1}$$

where $\nu_i = -1, 1$ is the instanton-anti-instanton index and $\boldsymbol{r}_i$ is the spatial coordinate of the ith instanton. The spatial coordinate contains three components, including the sublattice index [see Eq. (C4)].

The grand canonical Monte Carlo utilizes a Markov chain where each update consists of two stages: In the first stage, we update each coordinate of the instantons one by one, and in the second we change the total number of instantons.

The individual updates of the instantons' coordinates $(X_i, T_i) \to (\tilde{X}_i, \tilde{T}_i)$ are made according to the standard Metropolis algorithm. The proposal distribution is defined according to the following rules:

(1) The new value of the Euclidean time coordinate $\tilde{T}_i$ is chosen according to the Gaussian distribution, with standard deviation D_T, centered about the old coordinate. Here D_T is used as the set up parameter to tune the acceptance rate.

(2) The new type of the instanton $\tilde{\nu}_i$ is chosen between instanton (1) and anti-instanton (−1) value with equal probability.

(3) Proposals for the spatial coordinates and the sublattice index in $\tilde{X}_i$ are made simultaneously: We chose whether to move the instanton to one of the nearest-neighbors or to leave it at the same site. The probability is equal (25%) for each variant, since we have three nearest neighbors on the hexagonal lattice.

The Metropolis accept-reject step is made on the basis of the difference between the probability density for the old and the new configurations after the update of the coordinates for the ith instanton. According to Eq. (51), the probability to accept the new coordinates $(\tilde{X}_i, \tilde{T}_i)$ reads

$$P_i^{(1)} = \min\left(e^{-\Delta\mathcal{E}_i^{(1)}}; 1\right), \tag{D2}$$

where

$$\Delta\mathcal{E}_i^{(1)} = \sum_{j=1}^{N}(U^{(2)}(\tilde{X}_i, X_j, \tilde{T}_i - T_j) - U^{(2)}(X_i, X_j, T_i - T_j)). \tag{D3}$$

The update of the configuration size N is made according to the following algorithm:

(1) We choose whether to increase or decrease the configuration size N by one with equal probability.

(2) If we have chosen to increase the number of instantons, $N \to N+1$, we generate the new coordinates $(\tilde{X}_{\tilde{i}}, \tilde{T}_{\tilde{i}})$ with uniform distributions and insert them in the configuration at a random index $\tilde{i} = 1...N+1$. The combined total proposal probability $\mathcal{T}_{N\to N+1}$ can be written as

$$\mathcal{T}_{N\to N+1} = \frac{1}{N+1}\frac{1}{\beta}\frac{1}{2N_S}. \tag{D4}$$

This expression reflects the uniform distribution of the index $\tilde{i}$ of the new instanton, and also the uniform distributions of the spatial coordinates, Euclidean time coordinate, as well as the instanton-anti-instanton index. The probability of the inverse process corresponds to the simple choice of one instanton for deletion. Thus,

$$\mathcal{T}_{N+1\to N} = \frac{1}{N+1}. \tag{D5}$$

These expressions are then combined into the Metropolis probability for the acceptance of the new configuration with the additional instanton:

$$P_{\tilde{i}}^{(2)} = \min\left(\frac{\frac{1}{(N+1)!}e^{\tilde{\gamma}-\Delta\mathcal{E}_{\tilde{i}}^{(2)}}\mathcal{T}_{N+1\to N}}{\frac{1}{(N)!}\mathcal{T}_{N\to N+1}};1\right), \tag{D6}$$

where

$$\Delta\mathcal{E}_{\tilde{i}}^{(2)} = \sum_{j=1;j\neq\tilde{i}}^{N+1} U^{(2)}(X_{\tilde{i}}, X_j, T_{\tilde{i}} - T_j). \tag{D7}$$

Note, that in this case, unlike the case of Eq. (D2), we should take into account the changing factorials in Eq. (51). The final expression for the acceptance probability reads as

$$P_{\tilde{i}}^{(2)} = \min\left(\frac{e^{\tilde{\gamma}-\Delta\mathcal{E}_{\tilde{i}}^{(2)}}2N_S\beta}{N+1};1\right), \tag{D8}$$

(3) If we have chosen to decrease the number of instantons, $N \to N-1$, we select one of the instantons for removal (again with equal probabilities). Thus, the proposal probabilities for the forward and inverse transitions can be written as

$$\mathcal{T}_{N\to N-1} = \frac{1}{N} \tag{D9}$$

and

$$\mathcal{T}_{N-1\to N} = \frac{1}{N}\frac{1}{\beta}\frac{1}{2N_S}. \tag{D10}$$

Subsequently, the Metropolis acceptance probability can be obtained in the same manner as Eq. (D11),

$$P_{\tilde{i}}^{(3)} = \min\left(\frac{Ne^{-\tilde{\gamma}+\Delta\mathcal{E}_{\tilde{i}}^{(3)}}}{2N_S\beta};1\right), \tag{D11}$$

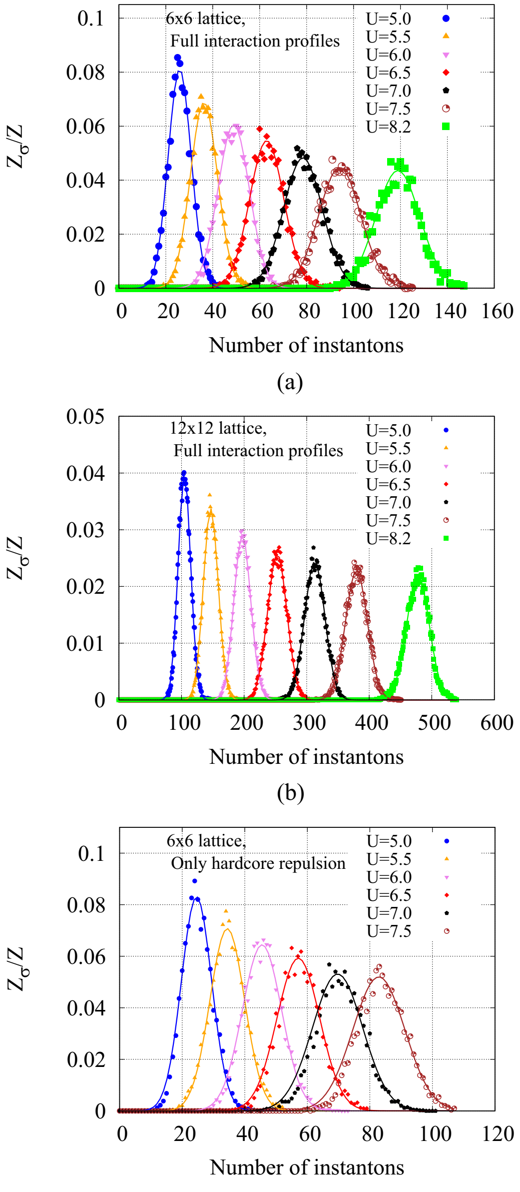

(a)

(b)

(c)

FIG. 26. The distribution of the number of instantons obtained from classical grand canonical Monte Carlo for instantons. The first two plots [(a), (b)] show the results for the model which incorporates the full interaction profile (obtained from the 6 × 6 and 12 × 12 lattices), while the last plot (c) shows the distribution for the case where only a hardcore repulsion between the instantons is taken into account. For all these calculations, $\beta\kappa = 20$. Gaussian fits are also included (shown with lines of the same colors as the corresponding data sets).

where

$$\Delta\mathcal{E}_{\tilde{i}}^{(3)} = \sum_{j=1,j\neq\tilde{i}}^{N} U^{(2)}(X_{\tilde{i}}, X_j, T_{\tilde{i}} - T_j), \tag{D12}$$

and $\tilde{i}$ is the index of the instanton selected for deletion.

As a test of the classical Monte Carlo, we plot the distributions of the instanton number for different interaction potentials (Fig. 26). As one can see, the distributions are

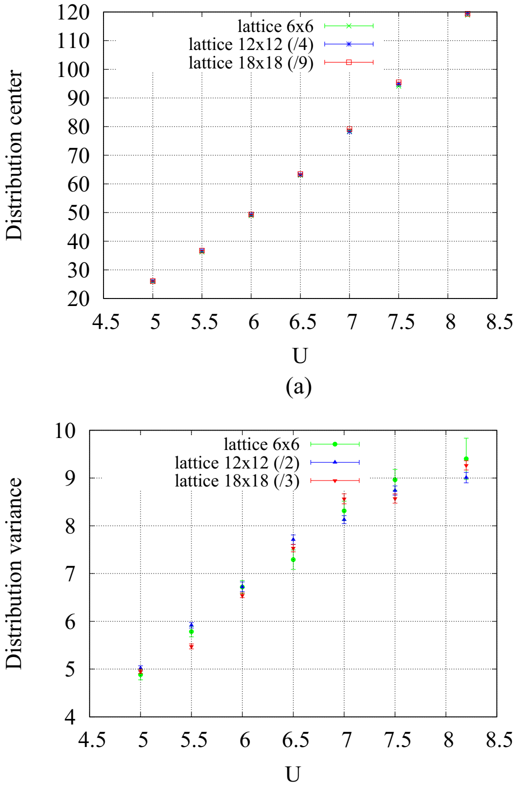

(a)

(b)

FIG. 27. (a) The average number of instantons, taken as the center of the distribution, from the classical grand canonical Monte Carlo simulations of the instanton gas model, taking into account only hardcore repulsion. (b) The variance of the distribution for the number of instantons from the same simulations. All data are obtained at $\beta\kappa = 20$. Note the rescaling of the data points for the 12×12 and 18×18 lattices.

perfectly fitted by Gaussian curves, in full agreement with the QMC data displayed in the Fig. 10. We also notice that the distributions are only slightly dependent on the exact form of the interaction profiles: one can compare Fig. 26(a), which corresponds to the full interaction profiles with Fig. 26(c), where only hardcore repulsion of the two instantons at the same site was taken into account.

We also check that the center of the distribution scales linearly with the lattice volume V [Fig. 27(a)] and the width of the distribution scales as $\sqrt{V}$ [Fig. 27(b)], again in agreement with the QMC data.

APPENDIX E: INSTANTONS AND THE GUTZWILLER PROJECTION

In this Appendix, we show how to establish a connection between the instantons and the ground-state wave function. To characterize the properties of the ground state following from the instanton approximation in a more intuitive way, we choose to work in the basis of occupation numbers. In this basis, the state at each site $\boldsymbol{x}$ is labeled by two numbers $n_{\boldsymbol{x},\mathrm{el}} = 0, 1$ and $n_{\boldsymbol{x},\mathrm{h}} = 0, 1$, which characterize the number of electrons and holes. Due to the fact that the creation-annihilation operators for electrons and holes, used in the Hamiltonian Eq. (1), are directly connected to those for electrons with spin up and spin down,

$$\hat{a}^\dagger_{\boldsymbol{x}} = \hat{a}^\dagger_{\boldsymbol{x},\uparrow}, \quad \hat{b}^\dagger_{\boldsymbol{x}} = \pm\hat{a}_{\boldsymbol{x},\downarrow}, \tag{E1}$$

where the sign in the latter equation alternates depending on the sublattice index, the states with fixed number of electrons and holes can be rewritten in terms of electrons with spin up and spin down. Here is an example for a single site:

$$\begin{aligned} |n_{\mathrm{el}} = 0; n_{\mathrm{h}} = 0\rangle &\rightarrow |n_\uparrow = 0; n_\downarrow = 1\rangle, \\ |n_{\mathrm{el}} = 0; n_{\mathrm{h}} = 1\rangle &\rightarrow |n_\uparrow = 0; n_\downarrow = 0\rangle, \\ |n_{\mathrm{el}} = 1; n_{\mathrm{h}} = 0\rangle &\rightarrow |n_\uparrow = 1; n_\downarrow = 1\rangle, \\ |n_{\mathrm{el}} = 1; n_{\mathrm{h}} = 1\rangle &\rightarrow |n_\uparrow = 1; n_\downarrow = 0\rangle. \end{aligned} \tag{E2}$$

Thus we can always return to the representation in terms of spin-up and spin-down electrons, despite the fact we are working in terms of electrons and holes for numerical convenience.

The general wave functions for each configuration $\{n_{\boldsymbol{x},\mathrm{el}}; n_{\boldsymbol{x},\,\mathrm{h}}\}$ can be obtained as

$$|n_{\boldsymbol{x},\mathrm{el}}; n_{\boldsymbol{x},\mathrm{h}}\rangle = \prod_{\boldsymbol{x}:n_{\boldsymbol{x},\mathrm{el}}=1} \hat{a}^\dagger_{\boldsymbol{x}} \prod_{\boldsymbol{x}:n_{\boldsymbol{x},\mathrm{h}}=1} \hat{b}^\dagger_{\boldsymbol{x}} |0\rangle, \tag{E3}$$

where $|0\rangle$ is the quantum state corresponding to the empty lattice. Here we consider only the states at half filling:

$$\sum_{\boldsymbol{x}} n_{\boldsymbol{x},\mathrm{el}} = \sum_{\boldsymbol{x}} n_{\boldsymbol{x},\mathrm{h}} = \frac{N_S}{2} = V. \tag{E4}$$

Our aim is to look at the decomposition of interacting ground state $|\Omega_{\mathrm{int}}\rangle$ (as it appears in the instanton gas approximation) in terms of the vectors $|n_{\boldsymbol{x},\mathrm{el}}; n_{\boldsymbol{x},\mathrm{h}}\rangle$. Thus, we need to compute the scalar products $\langle\Omega_{\mathrm{int}}|n_{\boldsymbol{x},\mathrm{el}}; n_{\boldsymbol{x},\mathrm{h}}\rangle$ within the instanton gas approximation. It is convenient to start with the vacuum state for the tight-binding Hamiltonian $|\Omega_{\mathrm{tb}}\rangle$, which is defined as a filled Dirac sea

$$|\Omega_{\mathrm{tb}}\rangle = \prod_{\boldsymbol{k};\sigma=1,2} \hat{c}^\dagger_{\boldsymbol{k},\sigma}|0\rangle, \tag{E5}$$

where

$$\hat{c}^\dagger_{\boldsymbol{k},1} = \sum_{\boldsymbol{x}} V^{(-)}_{\boldsymbol{x}}(\boldsymbol{k})\hat{a}^\dagger_{\boldsymbol{x}}, \quad \hat{c}^\dagger_{\boldsymbol{k},2} = \sum_{\boldsymbol{x}} V^{(-)}_{\boldsymbol{x}}(\boldsymbol{k})\hat{b}^\dagger_{\boldsymbol{x}} \tag{E6}$$

is the creation operator for the state with negative energy and $V^{(-)}_{\boldsymbol{x}}(\boldsymbol{k})$ is the corresponding eigenvector of single-particle tight-binding Hamiltonian for the momentum $\boldsymbol{k}$. Thus, we have

$$|n_{\boldsymbol{x},\mathrm{el}}; n_{\boldsymbol{x},\mathrm{h}}\rangle = \hat{A}(\{n_{\boldsymbol{x},\mathrm{el}}; n_{\boldsymbol{x},\mathrm{h}}\})|\Omega_{\mathrm{tb}}\rangle, \tag{E7}$$

where

$$\hat{A}(\{n_{\boldsymbol{x},\mathrm{el}}; n_{\boldsymbol{x},\mathrm{h}}\}) = \prod_{\boldsymbol{x}:n_{\boldsymbol{x},\mathrm{el}}=1} \hat{a}^\dagger_{\boldsymbol{x}} \prod_{\boldsymbol{x}:n_{\boldsymbol{x},\mathrm{h}}=1} \hat{b}^\dagger_{\boldsymbol{x}} \prod_{\boldsymbol{k};\sigma} \hat{c}_{\boldsymbol{k},\sigma}. \tag{E8}$$

Within the formalism of projective QMC [62,63], we consider the following combination of traces:

$$\begin{aligned} \mathcal{A} &= \left.\frac{\mathrm{Tr}\left(e^{-\hat{H}\beta}\hat{A}e^{-(\hat{H}_0 - E^{\mathrm{vac}}_{tb})\beta_P}\right)}{\mathrm{Tr}(e^{-\hat{H}\beta})}\right|_{\substack{\beta\to\infty \\ \beta_P\to\infty}} \\ &= \langle O_{\mathrm{int}}|\hat{A}|O_{\mathrm{tb}}\rangle\langle O_{\mathrm{tb}}|O_{\mathrm{int}}\rangle, \end{aligned} \tag{E9}$$

where β_P serves as the projection parameter, $\hat{H}$ is the full interacting Hamiltonian Eq. (1), $\hat{H}_0$ is its tight-binding part and $E^{\rm vac}_{\rm tb}$ is the energy corresponding to the tight-binding ground state $|\Omega_{\rm tb}\rangle$. After the Trotter decomposition Eq. (3) and HS decomposition Eq. (4) are made in both traces and the fermionic fields are integrated out, we arrive at the expression

$$\mathcal{A} \approx \sum_{\{\phi_{\rm inst}\}} A^{\rm el}_{\{\boldsymbol{x}:n_{\boldsymbol{x},\rm el}=1\}}(\{\phi\}) A^{\rm h}_{\{\boldsymbol{x}:n_{\boldsymbol{x},\rm h}=1\}}(\{\phi\}) \frac{\left|\det M^{\rm proj}_{\rm el}(\{\phi\})\right|^2}{\left|\det M_{\rm el}(\{\phi\})\right|^2}. \tag{E10}$$

Here $\det M_{\rm el}(\{\phi\})$ is defined in Eq. (7) and $\det M^{\rm proj}_{\rm el}(\{\phi\})$ is essentially the same except that it includes the additional exponent with projection:

$$\det M^{\rm proj}_{\rm el} = \det\left[I + e^{-\beta_P h}\prod_{\tau=1}^{N_\tau} D_{2\tau-1}D_{2\tau}\right]. \tag{E11}$$

The observables in Eq. (E10) are defined as the determinants of $V \times V$ matrices:

$$A^{\rm el}_{\{\boldsymbol{x}\}} = \begin{vmatrix} \tilde{g}_{\boldsymbol{x}_1\boldsymbol{k}_1} & \cdots & \tilde{g}_{\boldsymbol{x}_1\boldsymbol{k}_V} \\ \vdots & \dots & \vdots \\ \tilde{g}_{\boldsymbol{x}_V\boldsymbol{k}_1} & \cdots & \tilde{g}_{\boldsymbol{x}_V\boldsymbol{k}_V} \end{vmatrix}, \tag{E12}$$

where

$$\tilde{g}_{\boldsymbol{x}_i\boldsymbol{k}_j} = \sum_{\boldsymbol{y}} V^{(-)}_{\boldsymbol{y}}(\boldsymbol{k}_j) g_{\boldsymbol{x}_i\boldsymbol{y}}, \tag{E13}$$

with the fermionic propagator for electrons $g_{\boldsymbol{x}_i\boldsymbol{y}}$ computed at the zeroth time slice in the projected fermionic operator Eq. (E11). $A^{\rm h}_{\{\boldsymbol{x}\}}$ is the same with the exception of the complex conjugation of the fermionic propagator $g_{\boldsymbol{x}_i\boldsymbol{y}}$ in Eq. (E13).

The approximation in Eq. (E10) is due to the usage of the sum over only dominant saddle-point field configurations $\{\phi_{\rm inst}\}$ instead of the sum over all configurations of the auxiliary field. In fact, we will use only the field configurations with one or more instantons at the origin in order to better understand the properties of the ground state following from the presence of these semiclassical objects.

As the factor $\langle O_{\rm tb}|O_{\rm int}\rangle$ in Eq. (E9) is some constant which is independent of the occupation numbers $\{n_{\boldsymbol{x},\rm el}; n_{\boldsymbol{x},\rm h}\}$, we can use the non-normalized probability distribution

$$|\mathcal{A}|^2 \sim \left|\left\langle O^{\rm inst}_{\rm int}\middle|\{n_{\boldsymbol{x},\rm el}; n_{\boldsymbol{x},\rm h}\}\right\rangle\right|^2, \tag{E14}$$

following from the approximate expression Eq, (E10) to generate the configurations $\{n_{\boldsymbol{x},\rm el}; n_{\boldsymbol{x},\rm h}\}$ employing standard MC techniques. We finally obtain a set of basis vectors $|n_{\boldsymbol{x},\rm el}; n_{\boldsymbol{x},\rm\ h}\rangle$ distributed according to their weight within the interacting ground state $|O^{\rm inst}_{\rm int}\rangle$ corresponding to the instanton gas approximation.

To characterize this distribution, we plot the ratio of the frequencies

$$\mathcal{R}_{\boldsymbol{x}} = \frac{\mathcal{F}((\uparrow)_{\boldsymbol{x}}\quad \text{OR}\quad (\downarrow)_{\boldsymbol{x}})}{\mathcal{F}((\uparrow\downarrow)_{\boldsymbol{x}}\quad \text{OR}\quad (..)_{\boldsymbol{x}})}, \tag{E15}$$

where $\mathcal{F}((\uparrow)_{\boldsymbol{x}}\quad \text{OR}\quad (\downarrow)_{\boldsymbol{x}})$ corresponds to the frequency of the configurations $\{n_{\boldsymbol{x},\rm el}; n_{\boldsymbol{x},\rm h}\}$ with isolated spin up or spin down at the site $\boldsymbol{x}$ within the whole set of such configurations generated in the Monte Carlo process. $(\uparrow\downarrow)_{\boldsymbol{x}}$ denotes the configuration where both spin orientations are present on this site. $(..)_{\boldsymbol{x}}$ refers to the empty site. Both these configurations correspond to nonzero charge at the corresponding lattice site. The connection of spin-up and spin-down indices to the occupation numbers $\{n_{\boldsymbol{x},\rm el}; n_{\boldsymbol{x},\rm h}\}$ can be established via Eq. (E2).

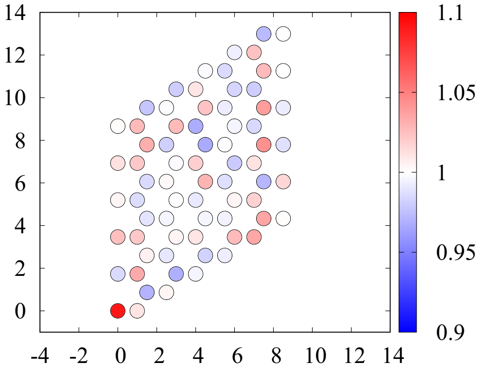

FIG. 28. The ratio of frequencies $\mathcal{R}_{\boldsymbol{x}}$ from Eq. (E15). These calculations were performed on the one instanton saddle on a 6×6 lattice with $\beta\kappa = 20$, $U = 6\kappa$, and $N_\tau = 512$. The instanton is located at the origin.

The map of frequencies $\mathcal{R}_{\boldsymbol{x}}$ is plotted in Fig. 28, where we generate configurations $\{n_{\boldsymbol{x},\rm el}; n_{\boldsymbol{x},\rm h}\}$ on the basis of a one-instanton saddle in Eq, (E10). We clearly see that the configurations with single spin (up or down) at the origin (where the instanton is located) are more frequent than the configurations with nonzero charge. This result directly corroborates the results displayed in Figs. 12 and 13 in the main text where the increased spin localization was observed with increasing instanton density.

Noting that the Gutzwiller projection can be used to describe this increasing localization, we check how well the ground state following from the saddle-point approximation can be described by the local Gutzwiller ansatz:

$$|\Omega_G\rangle = \hat{P}_{\boldsymbol{x}}(\eta)|O_{\rm tb}\rangle, \tag{E16}$$

where the operator $\hat{P}_{\boldsymbol{x}}$ is defined as

$$\hat{P}_{\boldsymbol{x}}(\eta) = \mathcal{N} e^{-\eta\hat{q}^2_{\boldsymbol{x}}}, \tag{E17}$$

and the normalization constant is obtained from the condition $\langle\Omega_G|\Omega_G\rangle = 1$:

$$\mathcal{N} = \sqrt{\frac{2}{e^{-2\eta}+1}}. \tag{E18}$$

We will consider several instantons located at a single spatial site but separated in Euclidean time. Thus, the spatial site $\boldsymbol{x}$ in Eq. (E16) coincides with the location of the center of the instantons in the saddle point field configuration. To characterize the projection Eq. (E16) in a simpler way, we rewrite it in terms of the particle number operators $\hat{n}_{\boldsymbol{x},\rm el}$ and $\hat{n}_{\boldsymbol{x},\rm h}$:

$$\hat{P}_{\boldsymbol{x}}(\eta) = -2(\hat{n}_{\boldsymbol{x},\rm el} + \hat{n}_{\boldsymbol{x},\rm h} - 2\hat{n}_{\boldsymbol{x},\rm el}\hat{n}_{\boldsymbol{x},\rm h})\sin\omega + \sqrt{2}\cos\left(\frac{\pi}{4} - \omega\right), \tag{E19}$$

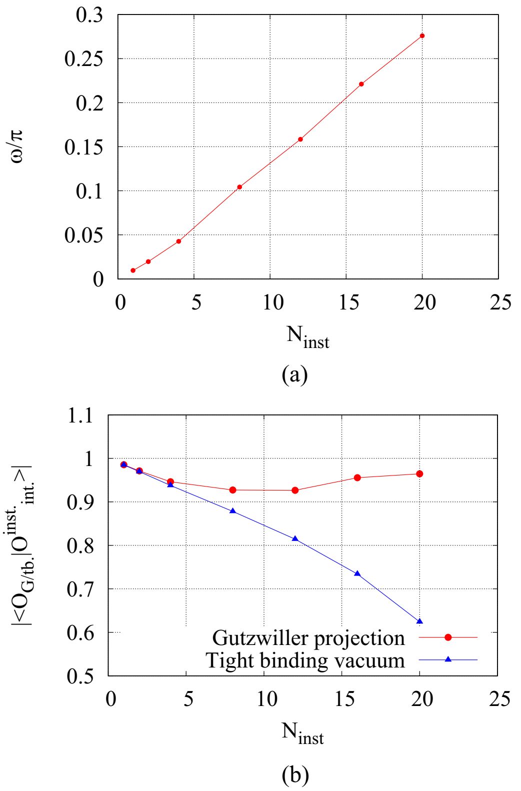

(a)

(b)

FIG. 29. (a) Dependence of the θ angle in the Gutzwiller projection for the optimal description of the N instanton saddle point. All instantons are located at the same spatial site and placed equidistantly in Euclidean time. (b) Overlap between two variants of probe wave function and the wave function following from the N-instanton saddle. These calculations were performed on a 6×6 lattice with $\beta\kappa = 20$, $U = 6\kappa$, and $N_\tau = 512$.

where

$$\cos\left(\frac{\pi}{4} - \omega\right) = \frac{1}{\sqrt{e^{-2\eta} + 1}}. \tag{E20}$$

The real parameter ω is tuned to maximize the overlap of the two states $\langle O^{\rm inst}_{\rm int}|\Omega_G\rangle = \langle O^{\rm inst}_{\rm int}|\hat{P}_x(\eta)|\Omega_{\rm tb.}\rangle$. This quantity can be obtained analogously to Eqs. (E9) and (E10), where the operator $\hat{A}$ is replaced by the operator $\hat{P}$ from Eq. (E20) and the observable $\mathcal{A}$ in Eq. (E10) is replaced by the corresponding observable for the operator $\hat{P}$. The unknown constant $\langle O_{\rm tb}|O^{\rm inst}_{\rm int}\rangle$ can be computed within the instanton gas approximation via the sum

$$\left|\langle O_{\rm tb}|O^{\rm inst}_{\rm int}\rangle\right|^2 = \sum_{\{\phi_{\rm inst}\}} \frac{\left|\det M^{\rm proj}_{\rm el}(\{\phi\})\right|^2}{\left|\det M_{\rm el}(\{\phi\})\right|^2}. \tag{E21}$$

As we are looking at the properties of the ground state corresponding to a set of instantons located at the same spatial site, only this multi-instanton saddle-point field configuration is included in the sum Eq. (E21).

The results are shown in Figs. 29(a) and 29(b). First, we look at the dependence of ω on the number of instantons [Fig. 29(a)]: the angle grows almost linearly. Second, we plot the dependence of the scalar product $\langle O_G|O^{\rm inst}_{\rm int}\rangle$ for this optimal ω on the number of instantons and compare it with $\langle O_{\rm tb}|O^{\rm inst}_{\rm int}\rangle$ [Fig. 29(b)]. As one can see, the overlap with the tight-binding vacuum quickly decays as the instanton number increases, but the overlap with the Gutzwiller Ansatz is stable and takes the value 0.95. Thus, we can conclude that the instanton gas approximation corresponds well to the Gutzwiller projection, with the added dynamics in Euclidean time allowing us to go beyond the properties of the ground state and to look at the properties of the spectral function, as in Fig. 2.

[1] P. W. Anderson, Phys. Rev. **124**, 41 (1961).
[2] W. Metzner and D. Vollhardt, Phys. Rev. Lett. **62**, 324 (1989).
[3] A. Georges, G. Kotliar, W. Krauth, and M. J. Rozenberg, Rev. Mod. Phys. **68**, 13 (1996).
[4] M. Imada, A. Fujimori, and Y. Tokura, Rev. Mod. Phys. **70**, 1039 (1998).
[5] Z. Fisk, H. Ott, T. M. Rice, and J. Smith, Nature (London) **320**, 124 (1986).
[6] P. Coleman, in *Handbook of Magnetism and Advanced Magnetic Materials* (John Wiley and Sons, Ltd., New York, 2007), Vol. 1, pp. 95–148.
[7] J. E. Hirsch, Phys. Rev. B **31**, 4403 (1985).
[8] E. Witten, arXiv:1009.6032.
[9] E. Witten, AMS/IP Stud. Adv. Math. **50**, 347 (2011).
[10] M. Cristoforetti, F. Di Renzo, and L. Scorzato (AuroraScience), Phys. Rev. D **86**, 074506 (2012).
[11] A. Alexandru, G. Basar, and P. Bedaque, Phys. Rev. D **93**, 014504 (2016).
[12] M. Ulybyshev, C. Winterowd, and S. Zafeiropoulos, Phys. Rev. D **101**, 014508 (2020).
[13] A. A. Belavin, A. M. Polyakov, A. S. Schwartz, and Y. S. Tyupkin, Phys. Lett. B **59**, 85 (1975).
[14] S. Coleman, The uses of instantons, in *The Whys of Subnuclear Physics*, edited by A. Zichichi, The Subnuclear Series Vol. 15 (Springer, Boston, MA, 1979).
[15] S. Vandoren and P. van Nieuwenhuizen, arXiv:0802.1862.
[16] S. K. Donaldson and P. B. Kronheimer, *The Geometry of Four-Manifolds* (Clarendon Press, Oxford, UK, 2007).
[17] G. 't Hooft, Phys. Rev. D **14**, 3432 (1976). [Erratum: **18**, 2199(E) (1978)].
[18] E. V. Shuryak, Phys. Rep. **61**, 71 (1980).
[19] ALF Collaboration, F. F. Assaad, M. Bercx, F. Goth, A. Götz, J. S. Hofmann, E. Huffman, Z. Liu, F. Parisen Toldin, J. S. E. Portela, and J. Schwab, SciPost Phys. Codebases **1** (2022).
[20] R. Blankenbecler, D. J. Scalapino, and R. L. Sugar, Phys. Rev. D **24**, 2278 (1981).
[21] S. R. White, D. J. Scalapino, R. L. Sugar, E. Y. Loh, J. E. Gubernatis, and R. T. Scalettar, Phys. Rev. B **40**, 506 (1989).
[22] F. F. Assaad and I. F. Herbut, Phys. Rev. X **3**, 031010 (2013).
[23] S. Sorella, Y. Otsuka, and S. Yunoki, Sci. Rep. **2**, 992 (2012).
[24] H. Fujii, S. Kamata, and Y. Kikukawa, J. High Energy Phys. 11 (2015) 078. [Erratum: 02 (2016) 036]..
[25] Y. Tanizaki, Y. Hidaka, and T. Hayata, New J. Phys. **18**, 033002 (2016) [hep-th].

[26] T. Kanazawa and Y. Tanizaki, J. High Energy Phys. 03 (2015) 044.

[27] A. Alexandru, G. Basar, P. F. Bedaque, G. W. Ridgway, and N. C. Warrington, J. High Energy Phys. 05 (2016) 053.

[28] F. Di Renzo and G. Eruzzi, Phys. Rev. D **97**, 014503 (2018).

[29] A. Alexandru, G. Basar, P. F. Bedaque, G. W. Ridgway, and N. C. Warrington, Phys. Rev. D **95**, 014502 (2017).

[30] A. Alexandru, P. F. Bedaque, and N. C. Warrington, Phys. Rev. D **98**, 054514 (2018).

[31] A. Alexandru, G. Basar, P. F. Bedaque, H. Lamm, and S. Lawrence, Phys. Rev. D **98**, 034506 (2018).

[32] A. Alexandru, P. F. Bedaque, H. Lamm, S. Lawrence, and N. C. Warrington, Phys. Rev. Lett. **121**, 191602 (2018).

[33] P. Buividovich, D. Smith, M. Ulybyshev, and L. von Smekal, Phys. Rev. B **99**, 205434 (2019).

[34] M. Fukuma, N. Matsumoto, and N. Umeda, Phys. Rev. D **100**, 114510 (2019).

[35] G. V. Dunne, J. Phys. A: Math. Theor. **41**, 304006 (2008).

[36] M. Ulybyshev, N. Kintscher, K. Kahl, and P. Buividovich, Comput. Phys. Commun. **236**, 118 (2019).

[37] E. V. Shuryak, *The QCD Vacuum, Hadrons and Superdense Matter*, 2nd ed. (World Scientific, Singapore, 2004).

[38] M. Raczkowski, R. Peters, T. T. Phùng, N. Takemori, F. F. Assaad, A. Honecker, and J. Vahedi, Phys. Rev. B **101**, 125103 (2020).

[39] G. Martinez and P. Horsch, Phys. Rev. B **44**, 317 (1991).

[40] R. Preuss, W. Hanke, and W. von der Linden, Phys. Rev. Lett. **75**, 1344 (1995).

[41] M. Brunner, F. F. Assaad, and A. Muramatsu, Phys. Rev. B **62**, 15480 (2000).

[42] B. Ponsioen, F. F. Assaad, and P. Corboz, SciPost Phys. **12**, 6 (2022).

[43] P. Béran, D. Poilblanc, and R. B. Laughlin, Nucl. Phys. B **473**, 707 (1996).

[44] F. Grusdt, M. Kánasz-Nagy, A. Bohrdt, C. S. Chiu, G. Ji, M. Greiner, D. Greif, and E. Demler, Phys. Rev. X **8**, 011046 (2018).

[45] R. Nandkishore, M. A. Metlitski, and T. Senthil, Phys. Rev. B **86**, 045128 (2012).

[46] M. Hohenadler and F. F. Assaad, Phys. Rev. Lett. **121**, 086601 (2018).

[47] B. Danu, Z. Liu, F. F. Assaad, and M. Raczkowski, Phys. Rev. B **104**, 155128 (2021).

[48] M. Raczkowski, B. Danu, and F. F. Assaad, Phys. Rev. B **106**, L161115 (2022).

[49] A. W. Sandvik, Phys. Rev. B **57**, 10287 (1998).

[50] K. S. D. Beach, P. A. Lee, and P. Monthoux, Phys. Rev. Lett. **92**, 026401 (2004).

[51] T. Schäfer, F. Geles, D. Rost, G. Rohringer, E. Arrigoni, K. Held, N. Blümer, M. Aichhorn, and A. Toschi, Phys. Rev. B **91**, 125109 (2015).

[52] E. Gull, P. Werner, X. Wang, M. Troyer, and A. J. Millis, Europhys. Lett. **84**, 37009 (2008).

[53] M. Randeria and E. Taylor, Annu. Rev. Condens. Matter Phys. **5**, 209 (2014).

[54] D. Pines, Z. Phys. B **103**, 129 (1996).

[55] www.gauss-centre.eu.

[56] Jülich Supercomputing Centre, J. Large-Scale Res. Facil. **5**, A171 (2019).

[57] S. Beyl, F. Goth, and F. F. Assaad, Phys. Rev. B **97**, 085144 (2018).

[58] S. R. White, R. L. Sugar, and R. T. Scaletar, Phys. Rev. B **38**, 11665 (1988).

[59] M. V. Ulybyshev and S. N. Valgushev, arXiv:1712.02188.

[60] M. V. Ulybyshev, P. V. Buividovich, M. I. Katsnelson, and M. I. Polikarpov, Phys. Rev. Lett. **111**, 056801 (2013).

[61] D. Smith and L. von Smekal, Phys. Rev. B **89**, 195429 (2014).

[62] F. Assaad and H. Evertz, in *Computational Many-Particle Physics*, edited by H. Fehske, R. Schneider, and A. Weiße, Lecture Notes in Physics, Vol. 739 (Springer, Berlin, 2008), pp. 277–356.

[63] S. Sorella, S. Baroni, R. Car, and M. Parrinello, Europhys. Lett. **8**, 663 (1989).